Reconstruction of bone-like structures through in-vitro mineralization of biogenic collagen substrates

Daviran, Deniz

Award date:
2021

Molecular Systems and Material Chemistry
Department of Chemical Engineering and Chemistry
Experimental work performed at Radboudumc, Nijmegen

Building Helix
Het Kranenveld 14
P.O. Box 513
5600MB Eindhoven

MSc. Thesis

Author:
Deniz Daviran

ID:
1377787

Reconstitution of bone-like structures through in-vitro mineralization of biogenic collagen substrates

D. Daviran

Supervisors:
Prof. dr. N.A.J.M. Sommerdijk
Dr. A. Akiva
R.H.M van der Meijden, MSc.

Graduation supervisor:
Prof. dr. J.C.M. van Hest

Graduation Committee:
Prof. dr. J.C.M. van Hest
Prof. dr. N.A.J.M. Sommerdijk
Dr. L.K.E.A. Abdelmohsen
R.H.M van der Meijden, MSc.

Date:
January 29th , 2021

Abstract

Bone is a composite material, formed by a collagen matrix embedded with platelets of hydroxyapatite. The intricate interplay between these two components are largely responsible for unique mechanical and biological properties of bone. The mechanism by which this mineralized matrix is formed is still largely unknown. Therefore, we aim to develop a reliable in vitro model that mimics natural biomineralization. Besides their scientific value in providing better insight into the mechanism of bone apposition, in-vitro models of collagen mineralization also possess engineering importance since they pave the way towards engineering bioinspired bone grafts and other mineralized scaffolds. In this work, biogenic collagen substrate was used to replicate the natural mineralization process and mimic the nano- and microstructure of bone. The distribution and extent of mineral deposition in tissue-based collagen scaffold and its evolution in collagen fibrils were studied with scanning electron microscopy, transmission electron microscopy and infrared spectroscopy. Furthermore, by isolating the organic and inorganic phase, the morphology and ultrastructural properties of each phase was separately studied in detail. The used workflow is meant to have minimal destructive effect on the samples in order to allow for multiple analyses to be applied to the same sample. With this work, we believe that we succeeded in mimicking the composition and structure of natural bone in this in vitro model.

Contents

Chapter 1. Introduction

1.1 Bone

Bone is a highly specialized connective tissue, evolved to provide optimal strength and protection.[1] This is achieved by optimizing bone tissues' unique cellular components and ultrastructural organization to provide maximum strength and impact resistance.[2] Bone tissue is built up of three interconnected phases: the living cellular components which regulate formation and remodelling of bone, the hydrated extracellular organic matrix, and the extracellular mineral phase.[2] The mineral phase is embedded within the extracellular organic phase, with the two phases forming a composite in which the organic phase provides toughness while the mineral phase is responsible for high strength of the bone tissue.

1.1.1 Formation and remodeling

Bone is a dynamic tissue, in which old bone is resorbed to be replaced with new bone. This remodeling is vital for the bone healing process and the optimization of bone strength.[3] The remodeling process is regulated by three types of bone cells: osteoblasts, osteoclasts and osteocytes.

Osteoclasts are multinucleated giant cells and remove old and weak bone through a multi-step complex pathway.[2] After the osteoclast attaches itself to old or damage bone tissue, the mineral of bone is dissolved through the release of H^+ ions and the organic matrix is removed by the release of collagen digesting proteins.[4]

Osteoblasts are fully differentiated cells and are considered the chief bone-forming cells. They synthesize and regulate the deposition of bone matrix and are responsible for production of the osteoid which is the nonmineralized extracellular matrix.[5] maintaining a balance between bone resorption and bone formation ensures the proper mechanical functioning of the bone tissue.[3]

Approximately 10% of osteoblasts on the bone surface gets trapped inside the newly formed bone matrix and subsequently differentiates into an osteocyte. Once an osteoblast transforms into an osteocyte, it loses its ability to secrete osteoid.[5] Osteocytes occupy spaces in bone called "lacunae" that are connected to each other via thin channels called "canaliculi". This interconnected system allows the osteocytes to communicate with other osteocytes and with the surface lining cells (the flat cells, covering the inactive bone surface). Hence, they can transmit signals to the surface and start the process of bone remodeling and formation.[4,5]

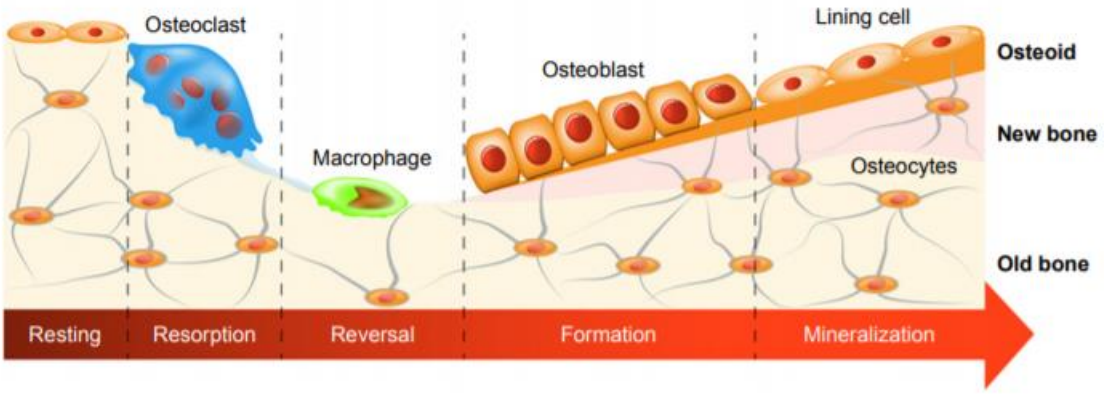

Figure 1. schematic representation of bone remodeling. Remodeling process is characterized by five phases: resting, resorption, reversal, formation and mineralization.[3]

1.1.2 Hierarchical structure

There are two main stages of bone formation which are referred to as primary and secondary osteogenesis. In the primary stage, the collagen fibril bundles are known to be more loose and mineralization happens faster and in an unorganized manner forming the "woven" bone microstructure. The rapid deposition of woven bone makes it an ideal solution for fracture repair. Hence, this stage of bone formation is considered a transient phase that lays the groundwork for subsequent formation of more structured bone.[6]

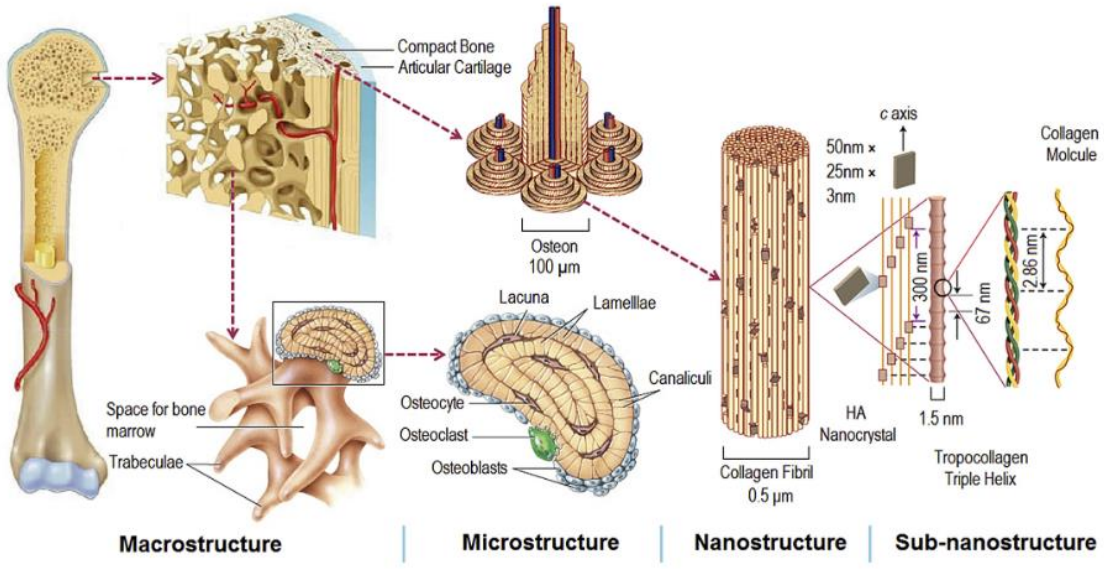

Figure 2. Bone hierarchical structure [7]

However, while discussing the hierarchical organization of bone, it is usually the secondary bone which is being described in terms of different hierarchical levels of structure.[1] This hierarchical structure and organization of bone is recognized to start from nano-scale (collagen molecules and hydroxyapatite crystals), all the way up to full bone (macro-scale).[8]

The primary woven bone remodels into the secondary bone, in order to achieve a more optimal structure. On the nanoscopic level this means that straight self-assembled collagen fibrils, with aligned platelets of hydroxyapatite are formed. On the micrometer level, these mineralized fibrils first come together and form fiber bundles, which subsequently form the parallel arrangements that make up the lamellae. These lamellae then arrange concentrically around the blood vessels and form osteons. Finally, on the macroscopic scale, the osteons either pack densely into compact bone or form a more porous structure which is known as spongy or cancellous bone.[1]

It should be kept in mind that the higher levels of bone structure are species-dependent and thus vary significantly between organisms. Whereas the nanostructural level of organization is the foundation of all types of secondary bone. Consequently, understanding the properties of any type of bone requires careful examination of this basic level of organization, the nanostructured array of hydroxyapatite crystals embedded within the collagen matrix.[1]

1.1.3 Composition

Of the previously mentioned mineralized collagen phase, the mineral phase contributes 60-70 wt.%, approximately 20-30 wt.% accounts for the extracellular organic matrix and the remaining 10% is

water.[8] The mineral phase consists of calcium phosphate hydroxyapatite crystals substituted with carbonate and trace elements like sodium, potassium, magnesium, fluoride, and chloride.[9] In the organic phase, the main protein is fibrillar collagen type I which accounts for ~90% of the total organic content in bone. The remaining 10% consists of a set of non-collagenous acidic proteins (NCPs) which contain highly charged residues such as aspartic acid and glutamic acid residues.[1] Despite low concentration, these proteins are expected to play an important role in controlling and regulating the mineralization process.

1.2 Bone mineral

The inorganic phase of bone is composed of calcium and phosphate in the form of hydroxyapatite (HA). Stoichiometric HA has the formula $Ca_{10}(PO_4)_6(OH)_2$, and a hexagonal crystal lattice. However, HA in bone is strongly substituted. These substitutions mostly occur in the form of divalent anions like CO_3^{2-} and HPO_4^{2-} or the substitution of calcium with other cations such as magnesium or strontium.[10] Due to high levels of carbonate substitution, the bone mineral is often known as nonstoichiometric carbonated hydroxyapatite (cHA).[11] The large amount of substitutions in bone results in minerals with reduced crystallinity.

Bone crystals are the smallest crystals known in nature.[8] In fact, the platelet-shaped cHA minerals in bone have been shown to be 50-100 nm long, 25-50 nm wide and 3-5 nm thick. Resolving these small crystallites has proven to be very difficult in the presence of the collagenous matrix. Therefore, attempts have been made to isolate the bone mineral for better visualization of the ultrastructure. *Shah et al.* used a simple deproteinization technique (also used in this work) to study the organization of mineral platelets on the floor of osteocyte lacunae in sheep cancellous bone.[12] They were able to clearly visualize the repeating motifs of mineral bundles that stacked both laterally and tip-to-end to form motifs that are about $1\mu m$ long and 70-100 nm wide. This was not feasible with the organic phase being present.

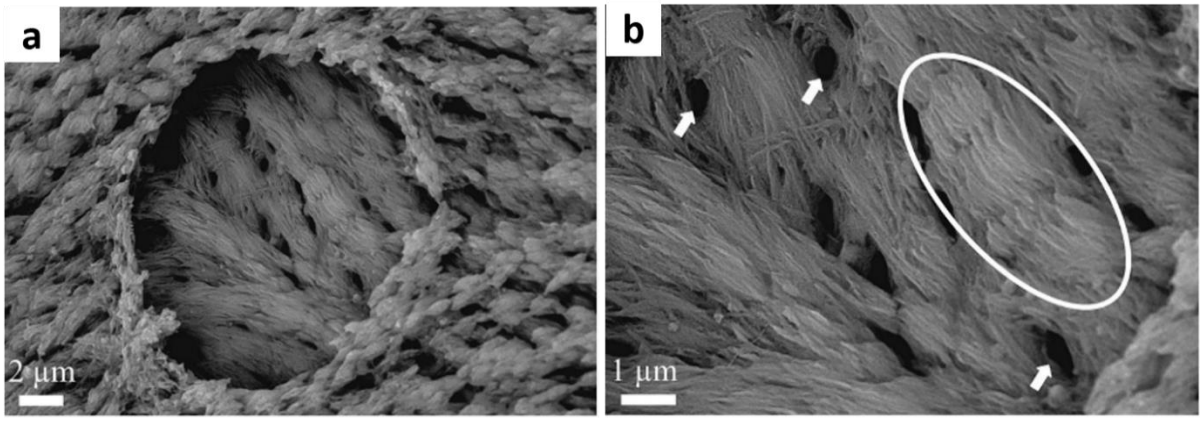

Figure 3. SEM micrographs of a deproteinized osteocyte lacuna at low (a) and high (b) magnification. The area outlined by the white ellipse displays bundles of mineral platelets stacked laterally and tip-to-end. The white arrows point to the holes that are probably left behind by the osteocyte dendrites.[12]

In another study, they performed the same deproteinization technique on rat skulls focusing on the cranial sutures due to the fact that these areas are known to be primary sites of bone formation in the skull. They observed a correlation between mineral age and morphology and claimed that bone mineral goes through a transient phase of discrete marquise-shaped motifs that later on become interconnected and form a continuous phase.[13] Our work demonstrates the extension of this research to human cortical bone.

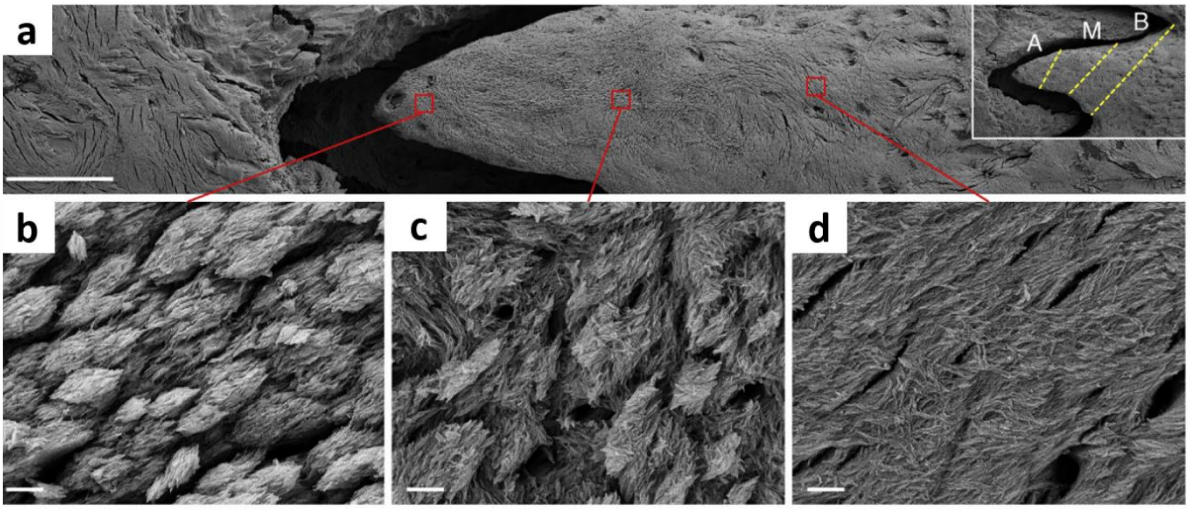

Figure 4. Evolution of bone mineral morphology in the apical (A), middle (M) and basal (B) third of the finger-like projection in rat skull cranial sutures. Moving from the apical third towards the basal third, mineral morphology changes from discrete marquise-shaped motifs to an interconnected continuous mesh. Scale bar in a=100 μm, scale bars in b,c,d=1μm.[13]

1.3 Organic phase

1.3.1 Collagen type I structure

The term "Collagen" describes a large family of proteins which make up most connective tissues. Different types of collagen exist in different tissues, each optimized to fulfill its specialized role.[14] Collagen is the most abundant structural protein and makes up one-third of the total amount of proteins present in human body. It is the dominant constituent of the extracellular matrix (ECM). So far, 28 different types of collagen have been identified.[15]

As stated before, 90% of the bone organic component is collagen type I.[16] The defining feature of collagen molecule is a structural motif in which two $\alpha 1$ and one $\alpha 2$ polypeptide (protocollagen) strands form a left-handed (alpha)-helical conformation with a one-residue stagger to form a right-handed triple helix (procollagen)(fig 5). In order for this triple helix to be tightly packed, it is essential that every third residue in the amino acid sequence of the polypeptide strands be Glycine, resulting in a repeating XaaYaaGly sequence. In principle, Xaa and Yaa can be any amino acid. However, these positions are often filled by Proline and Hydroxyproline respectively, making ProHypGly the most common triplet in collagen.[17] The repetition of this tripeptide sequence forms the smallest building block of the collagen molecule (protocollagen strand).

Each procollagen has non-triple helical domains at each end (propeptides) that direct the triple-helix folding of the collagen molecule. Once the triple-helix is formed, these N- and C-terminal domains are cleaved by specific proteases leading to the formation of tropocollagen. This cleavage is necessary for the initiation of fibrillogenesis process.[15] Tropocollagen still contains some shorter non-helical portions at both ends (telopeptides) which are essential for proper fibrillogenesis. Furthermore, these telopeptides have an important role in stabilizing mature collagen fibrils since they allow for crosslinking of the molecules.

Tropocollagen is about 300 nm long and less than 2 nm in diameter and has the unique property of actually being unstable at body temperature.[15] This property makes it a highly reactive molecule that can easily undergo spontaneous fibrillogenesis in an entropy-driven process which has a stabilizing effect on the triple helices.[14] The product of the assembly is stabilized by polar, hydrophobic and other non-covalent interactions. These interactions define the staggered localization of adjacent collagen

molecules. The lateral stacking results in a short gap space of about 40 nm between the end of each molecule and the beginning of the next one (fig 5) when looking in the longitudinal direction of the molecule. Lateral stacking of 5 tropocollagen strands, forms a collagen defining periodic structure with a period of about 67 nm called the D-spacing. This D-spacing is divided into a gap and overlap zone forming the collagen microfibril which can be observed using electron microscopy.

Finally, further stabilization is ensured by enzymatic crosslink formation through lysyl oxidase initiation on the telopeptides resulting in the formation of the collagen fibrils.[16]

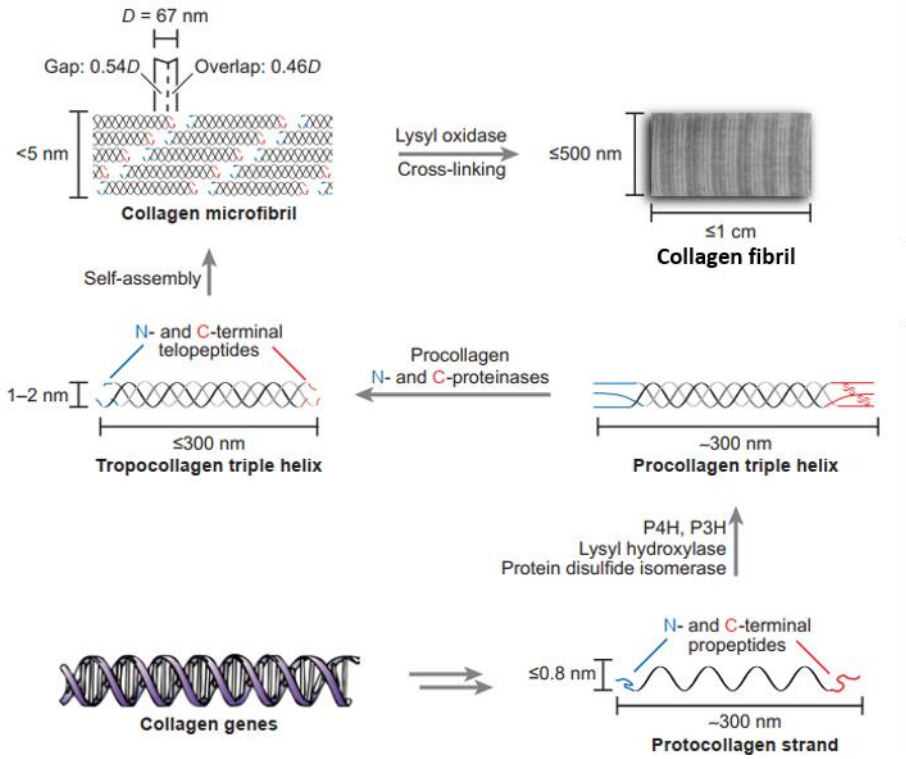

Figure 5. Hierarchical structure of collagen [15]

1.3.2 Collagen organization in lamellar bone

Organization and orientation of the collagen fibrils in bone has biomechanical significance. To study this, *Reznikov et al.* used a focused ion beam (FIB)/SEM to sequentially remove thin layers of about 10nm from the surface of demineralized human lamellar bone and demonstrated that there are both ordered and disordered collagenous motifs present in lamellar bone, with the disordered motifs filling the space in between two successive ordered motifs.[18] As for the ordered motifs, different array patterns were observed with the most common one being highly anisotropic patterns with all the collagen fibrils aligned along their long axis (fig 6a). Another observed pattern was the fibrils gradually changing their direction (fig 6b). This pattern is known as “twisted plywood” and is common in lamellar bone. As for the disordered motif, collagen fibrils are randomly oriented and as mentioned before, fill the spaces between two consecutive ordered layers (fig 6c).[6]

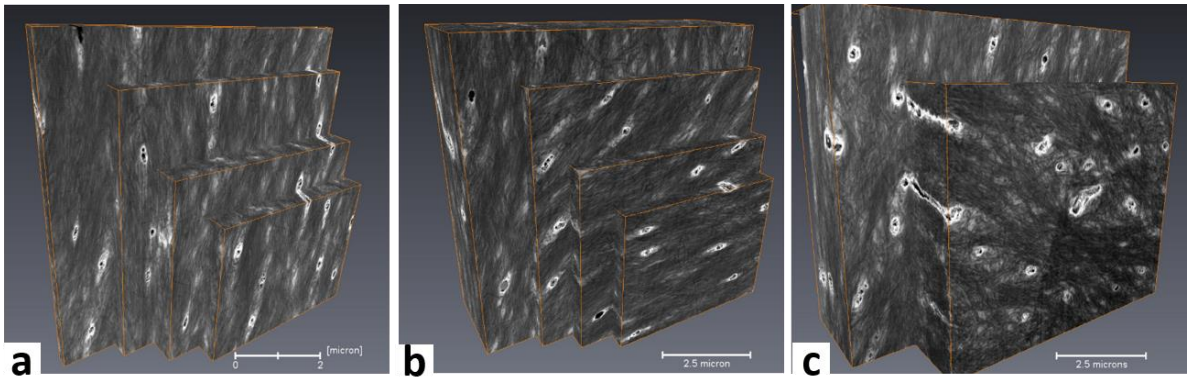

Figure 6. reconstruction of different organizations of collagen fibrils in human lamellar bone.[18] *(a) unidirectional array, (b) twisted plywood array (c) disordered array. Scale bars: a=2 μm , b,c=2.5 μm*

1.4 Collagen mineralization

The mineralization of the collagen matrix is of great importance for the final mechanical properties of bone tissue. Therefore, understanding the unique properties of bone ultimately requires insight into the process and mechanism involved in biomineralization. Additionally, gaining a better understanding of the intricate interplay between collagen and bone mineral, is imperative for success in research areas such as understanding mineralization-related diseases and developing bioinspired synthetic bone grafts.

1.4.1 Structure of mineralized collagen fibril

Studies on the mineralized collagen fibril have shown that the platelet-shaped cHA crystals are oriented with their c-axis parallel to the long axis of their host collagen fibril (fig 7b, 7c).[19] Furthermore, by applying high voltage electron microscopy and tomography on mineralizing avian tendon, *Landis et al.* demonstrated that the mineral platelets residing within the fibril show a preference for the gap zones [20] and later on extend into the overlap zones.[21]

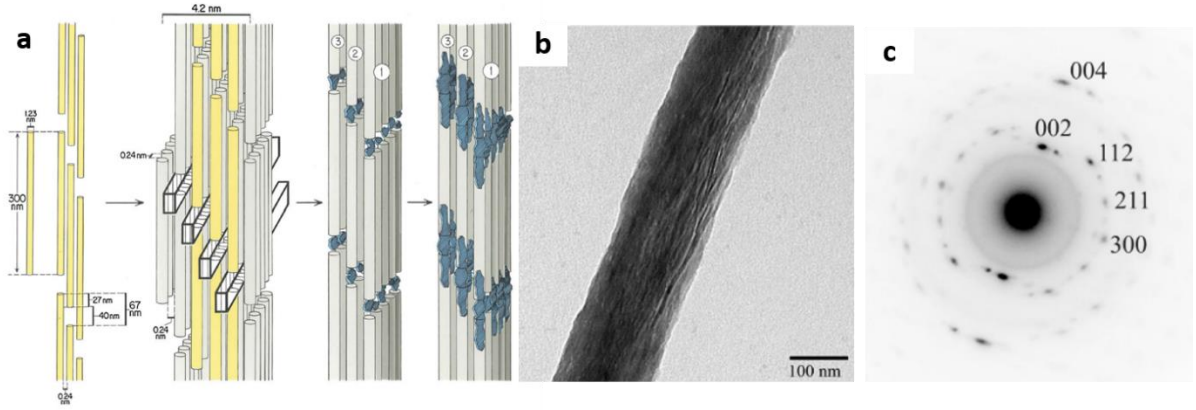

Figure 7. (a) schematic representation of collagen mineralization. Mineralization starts in the gap zones and then extends into overlap zones [1]*. (b) TEM image of a collagen fibril mineralized for 16h, (c) the diffraction pattern of the fibril in (b) showing the [002] plane reflection along the long axis of collagen.*

Alongside the growing evidence for this intrafibrillar mineralization, development of techniques like ion-milling for preparation of ultrathin sections of mineralized tissue allowed for high resolution TEM imaging of the mineralized tissue. Using this method, *Schwarcz et al.* [22] showed that the majority of the bone mineral exists in the extrafibrillar space and recently, *Reznikov et al.* established different morphological patterns for these extrafibrillar minerals using STEM tomography.[23]

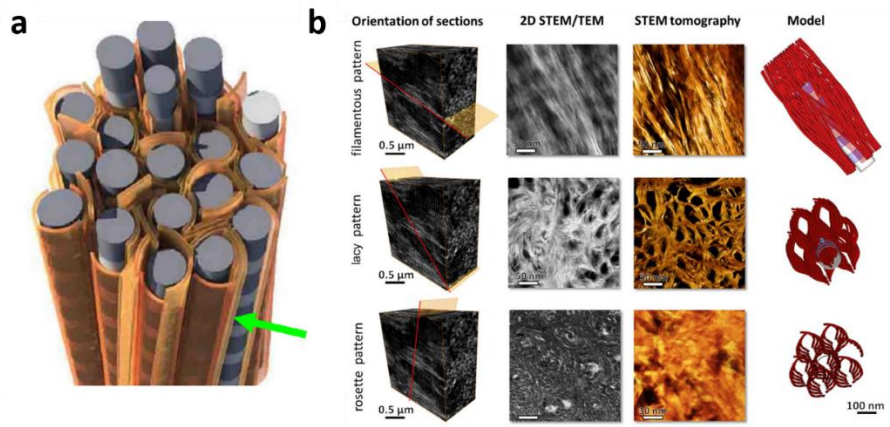

Figure 8. (a) Model proposed by Schwarcz et al. [22] displaying stacks of minerals around the collagen fibrils. the green arrow points to the stacks of minerals outside the fibrils enveloping them. (b) Different organizational patterns for mineral crystals around the collagen fibrils by Reznikov et al. [23]

1.4.2 Collagen mineralization in-vivo

It has long been accepted that mineralization of collagen does not involve a traditional nucleation and precipitation of apatite crystals. *Beniash et al.*[24] showed that mineral formation in enamel occurs through a transient amorphous calcium phosphate (ACP) phase which later on transforms into apatitic crystals. *Mahamid et al.* [25] were able to demonstrate that collagen mineralization occurs through a similar mechanism as well. Using cryo-SEM, they were able to follow the mineralization of native zebrafish fin bones and showed that initially, the growth zones contain globular entities of ACP which fuse into the collagen fibrils at the mineralization front and later on are transformed into crystalline platelets of cHA.

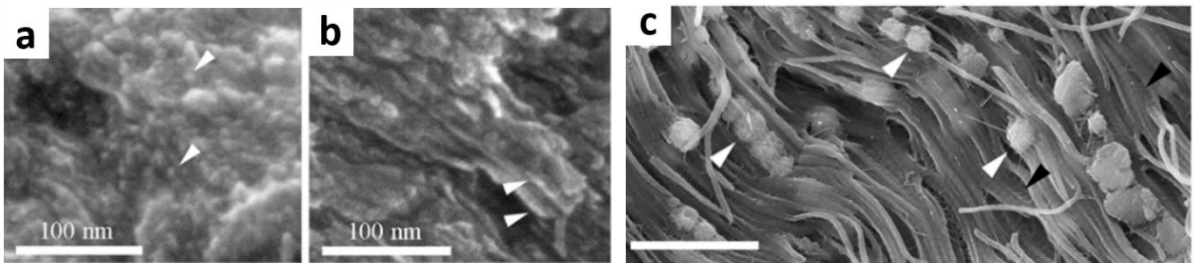

Figure 9 Cryo-SEM images representing mineralization of native zebrafish fin bones.[25] (a) newly mineralized bone showing spherical particles (arrow-heads), (b) mature bone showing mineral phase in the shape of thin platelets (arrow-heads), (c) mineral bearing globular entities (white arrow-heads) fusing with the collagen fibrils (black arrow-heads) at the growth zone. Scale bar in c=1 µm

1.4.3 Role of non-collagenous proteins

Attempts to replicate these structures in-vitro, quickly revealed that adding only collagen to a oversaturated solution of calcium phosphate does not result in bone-like mineralization. More importantly, none of the attempts made were able to achieve intrafibrillar mineralization[26] but merely resulted in apatite precipitation in solution and on the surface of collagen fibrils.[27] These results were attributed to the lack of non-collagenous proteins (NCPs) in the attempted remineralization processes.[28] Despite the low percentage of NCPs in bone tissue, there is a wide variety of NCPs in bone and still much is unknown about the exact function and role that each one of them plays in bone formation.[6] Nevertheless, some of these NCPs like osteopontin and bone sialoprotein are thought to play a major role in biomineralization.[29] Investigation of the properties and structural features of these proteins allowed researchers to explore alternative materials to induce intrafibrillar mineralization.

1.4.4 In-vitro models of collagen mineralization

Mineralization-related NCPs showed a strong polyelectrolytic nature and were highly negatively charged due to abundant carboxylate groups in their aspartic and glutamic residues.[29,30] *Olszta et al.* used poly aspartic acid (polyAsp) as a substitute for these NCPs in-vitro and were able to achieve intrafibrillar mineralization. They proposed that by forming a complex with ACP, polyAsp is able to stabilize the ACP in a liquid-like, highly-hydrated phase and inhibit its nucleation long enough to allow infiltration into the collagen fibril. This method is known as the polymer induced liquid precursor (PILP) process [1] and will also be used in this research.

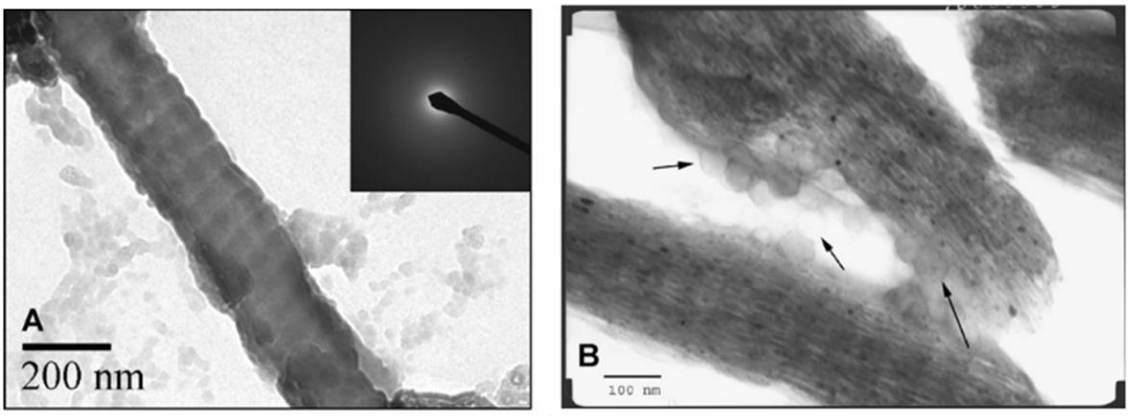

Figure 10. (A) TEM image of a collagen fibril removed from Cellagen spong during early stages of mineralization with PILP process.[1] The fibrill appears enriched with ACP. The SAED pattern in the inset shows a diffuse ring whoch is characteristic of the ACP mineral phase (B) TEM image of a collagen fibril after remineralization with PILP process displaying parallel dark stripes of minerals parallel to the collagen long access presumably inside the fibril. The arrows point to the remnants of the liquid precursor phase containing ACP outside the fibrils.[1]

To better understand the mechanism of fibril infiltration, *Nudelman et al.*[27] used cryo-TEM tomography and showed that the gap zones in collagen are positively charged regions, making them a preferable location for the infiltration of the negatively-charged polyAsp-ACP complex. Additionally, by replacing polyAsp with fetuin, they showed that the main role of these molecules is stabilizing the ACP. While polyAsp itself enters the collagen fibril, fetuin has a higher molecular weight and cannot penetrate the fibril. Nevertheless, intrafibrillar mineralization still occurs proving that the infiltration of the polymer itself into the collagen fibril is not a requirement.[27] This variation of the PILP process is known as "mineralization by inhibitor exclusion".[31]

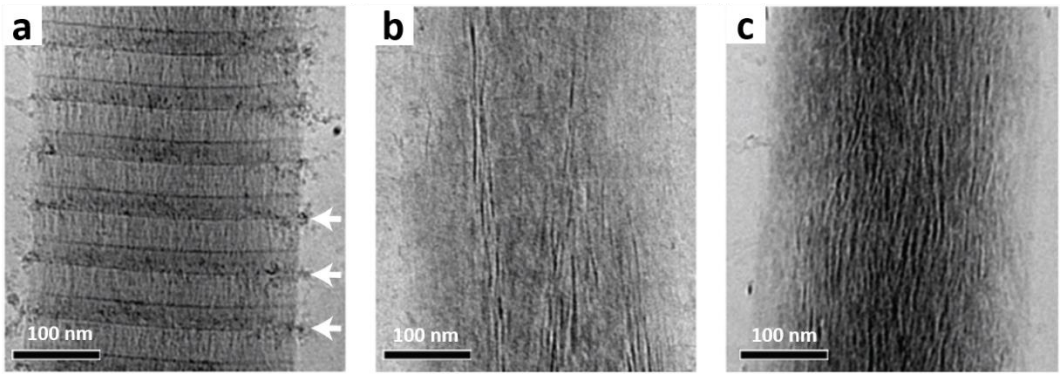

Figure 11. Cryo-TEM images of collagen mineralization after (a) 24h (b) 48h and (c) 72h using polyAsp as the process directing agent. The white arrows pinpoint the ACPs that are about to infiltrate the fibril at the gap zones. [27]

Many different aspects of the PILP process have since been investigated. *Thula et al.*[32] compared different anionic directing agents such as poly Aspartic acid (polyAsp), poly glutamic acid (PGLU), poly acrylic acid (PAA) and polyvinylphosphonic acid (PVPA) and concluded that polyAsp and combination of polyAsp/PGLU leads to the highest mineral content as well as bone-like nanostructures.[32] Additionally, Nudelman et al. [33] showed that the concentration of the directing agent directly controls the rate of collagen mineralization, with lower concentrations yielding faster mineralization.

Following the successful results of mimicking biomineralization in reconstituted collagen, many researches were focused on mineralizing natural collagen substrates by demineralization of bone[34], turkey leg tendon [35] and periodontal ligament.[36] In terms of substrate packing density, turkey leg tendon lies in between collagen sponges and lamellar bone, meaning that it is denser than a collagen sponge but more loosely packed than lamellar bone.[35] In their attempt to remineralize turkey leg tendon, *Gower et al.* [35] used the PILP process with polyAsp and observed a layer of mineral coating covering collagen fibrils after 6 days. Subsequently, they treated the remineralized samples very briefly with HCL in order to remove this external coating and expose the mineralized collagen fibrils. The presence of mineral was confirmed via synchrotron x-ray diffraction.

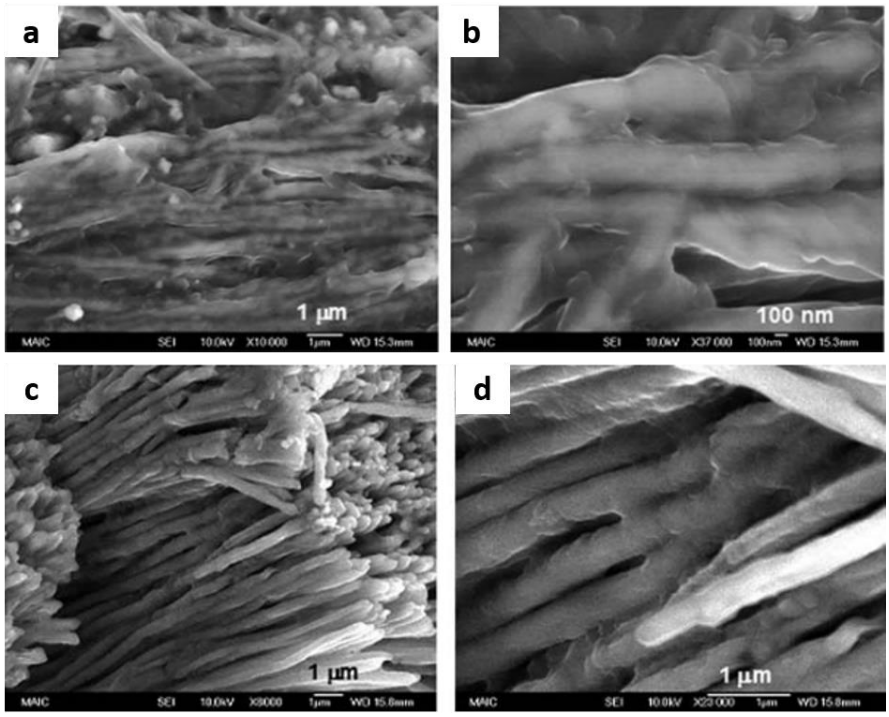

Figure 12. SEM micrographs of turkey leg tendon mineralized for 6 days using polyAsp as process directing agent. (a,b) Low and high magnifications of mineralized collagen fibrils with an external mineral coating, (c,d) Low and high magnification of mineralized fibrils after treatment with HCl to remove the external mineral coating. [35]

Other than proving the effectiveness of the PILP process remineralization of demineralized periodontal tissue, *Lausch et al.*[36] proved that extracellular matrix retains enough information to selectively induce mineralization in natively mineralized tissue (cementum and dentin) and not the periodontal ligament.

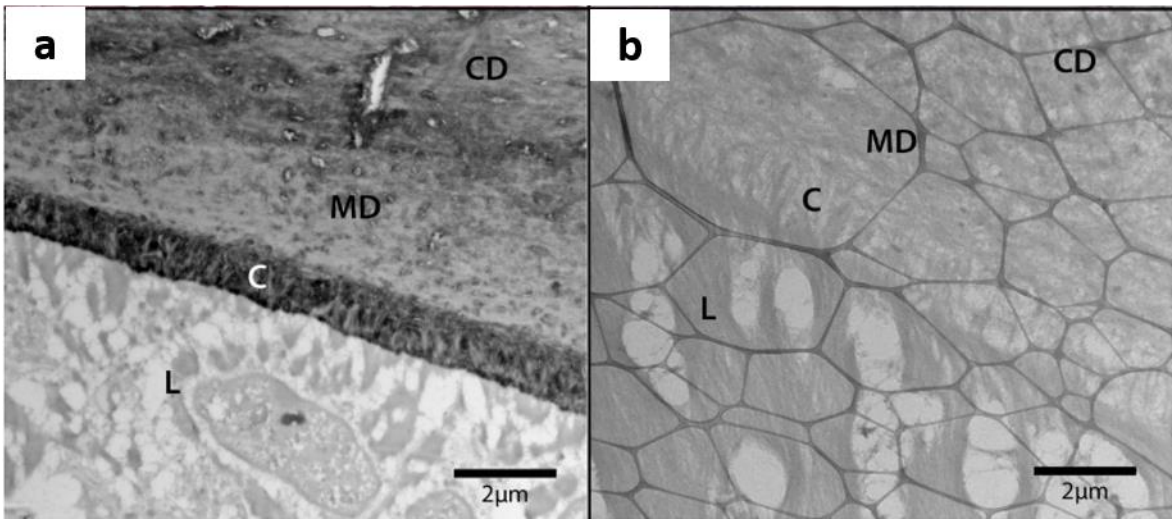

Figure 13. TEM images of 210 nm-thin demineralized (b) and remineralized (a) periodontal tissue. The periodontal ligament (L) has remained non mineralized while the cementum (c) and mantle dentin (MD) are mineralized. [36]

Finally, *Rodriguez et al.*[37] compared remineralization of demineralized bovine bone slices with and without incorporating the PILP process. They were able to prove the presence of mineral components in the remineralized specimen by EDS analysis. However, their results did not include any details regarding the ultrastructure of the remineralized fibrils. However, in another study, they applied the same PILP process on slices of manatee bone and were able to achieve bone-like architecture.[38] Our research has many aspects in common with this study.

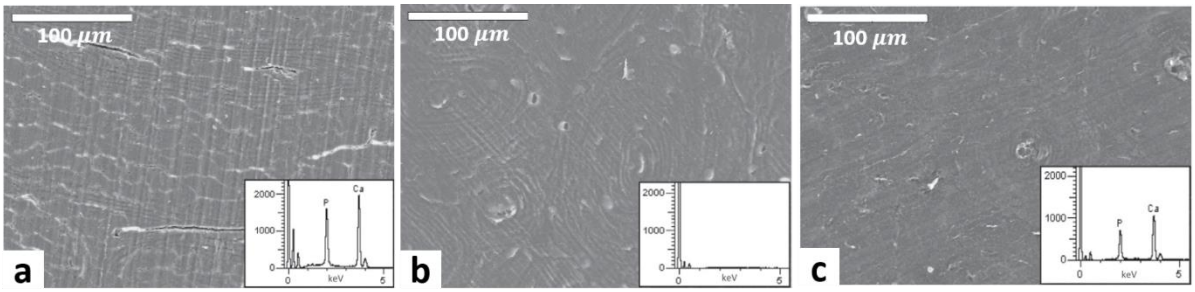

Figure 14. SEM micrographs of (a) natural (b) demineralized and (c) 7-day remineralized bovine bone using polyAsp as the process directing agent [37]

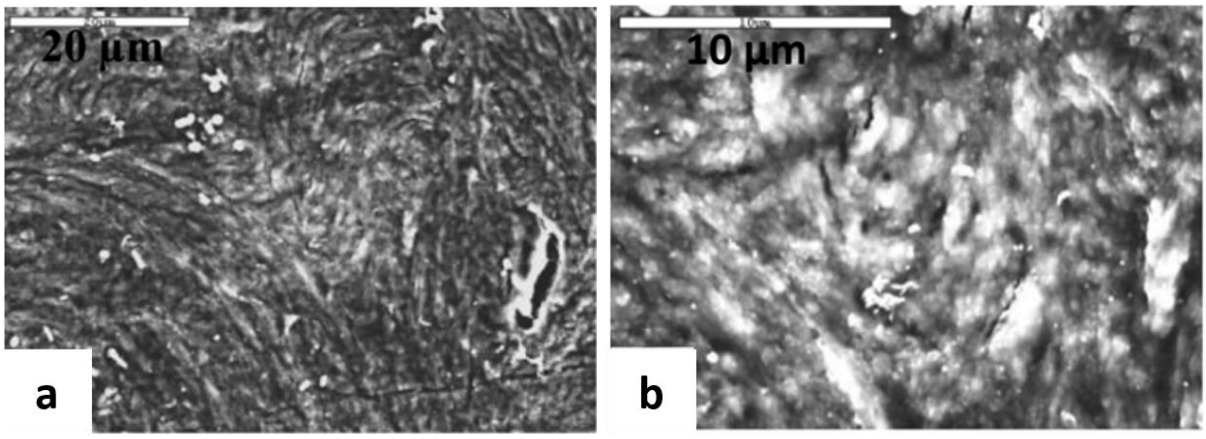

Figure 15. SEM micrographs displaying (a) Low and (b) high magnifications of manatee bone surface remineralized for 7 day via PILP process with polyAsp as the process directing agent [34]

1.5 Project aim

The aim of this project is to replicate the mineralization of bone matrix in-vitro and mimic the nano- and microstructure of native bone in terms of the nature of replicated minerals and collagen-mineral relation. Achieving a bone-like micro- and nano-structure could serve as a platform for production of any type of collagen-based mineralized substrate such as bone grafts and dental implants. Moreover, an optimized and reliable workflow for replication of the mineralization process would aid in conducting similar experiments and thereby pinpoint where the process fails in mineralization-related diseases, why it fails and how it could be remedied.

To this end, using analytical techniques, dynamics of bone demineralization and physical properties of the replicated mineral phase will be investigated. Furthermore, microscopic techniques will be applied to study orientation, morphology and ultrastructure of the isolated organic and inorganic phase as well as mineral formation and distribution both in collagen fibrils and across the bulk of the specimen. The characterization techniques and their order of application will be chosen in a manner to have the least destructive effect on the samples which in turn will make the investigation of rare diseased samples based on this method, practical.

1.6 Workflow

The roadmap that will be followed in this work is shown below. First, we will study the mineral phase of native bone by applying a simple deproteinization technique to isolate the inorganic phase. Afterwards, we will perform demineralization on the native bone and then remineralize the isolated collagen substrate both on a TEM grid and across the bulk. At each step, proper characterization methods will be applied to validate the results.

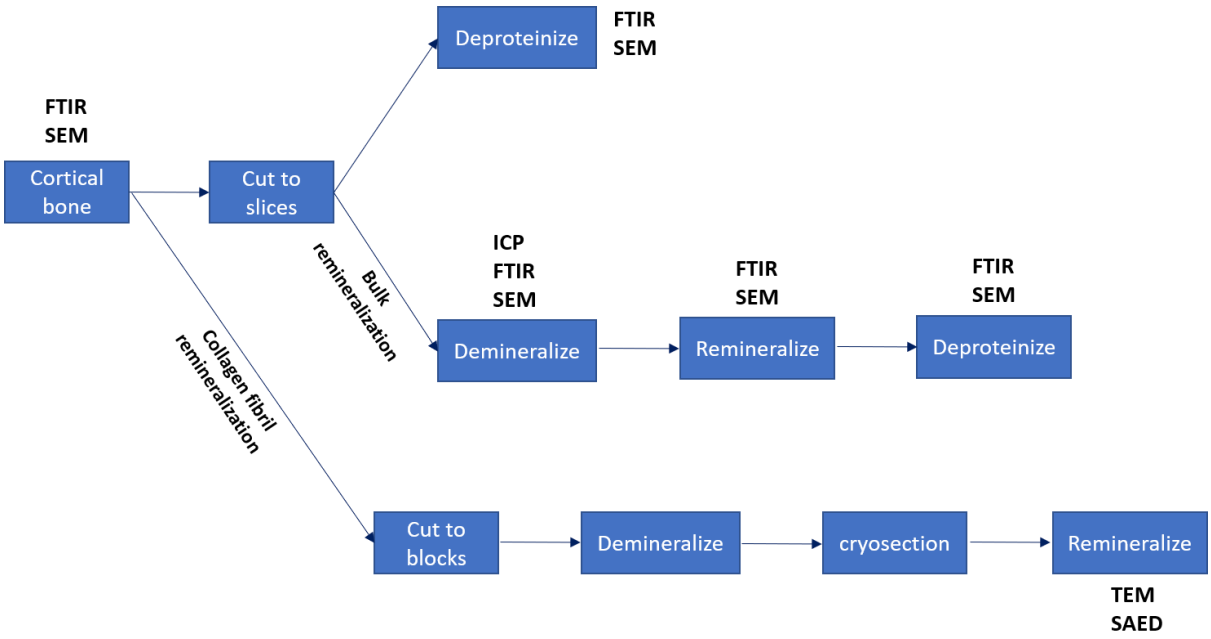

Flow chart of the experimental steps followed for remineralization of biogenic collagen

Chapter 2. Characterization techniques

The earlier mentioned hierarchical structure of bone leads to its heterogeneous structure across different length scales. Therefore, a wide variety of techniques have been developed to resolve structural details and obtain compositional information about bone. In this work, we have mainly applied scanning electron microscopy for structural analysis and infrared spectroscopy for characterization of the mineral phase. Furthermore, transmission electron microscopy coupled with selected area electron diffraction is applied to study mineralization on fibrillar level and determine orientation. Finally, inductively coupled plasma spectroscopy is used to study the dynamics of demineralization. In this chapter, a summary of the theory behind each applied technique is presented with a more in-depth focus on SEM and FTIR as they are the most extensively used techniques in this work.

2.1 Scanning Electron Microscopy

A scanning electron microscope (SEM) is a microscope which uses electrons in order to create an image of a specimen. By using electrons instead of light a higher resolution can be achieved and thus more details can be analysed compared to traditional light microscopy. These images can contain a variety of information regarding morphology, structural and chemical properties.[39]

The imaging principle of a SEM is based on a highly focused electron beam which is scanned over a surface to generate an image. The electrons are generated by emission from an electron source and accelerated to by applying a negative potential (ranging from 0.1 – 30 keV). After emission, and acceleration, of the electrons the electrons are focused by passing the electron beam through several apertures and magnetic coils to reduce the beam diameter. This highly focused electron beam scans the surface of the specimen point by point. At each point, the beam interacts with the specimen and generates outgoing electrons with different energies which are then collected by different electron detectors. Finally, the detectors digitize the recorded signal which are translated into the grey level at each x-y location corresponding to the scanning point on the specimen surface. Conventionally, SEM needs to operate in high vacuum ($<10^{-5}$ Pa) in order to prevent the interaction of both the electron beam and the produced electrons with air molecules and prevent their scattering.[40] Fig 16a shows schematics of the SEM instrument.

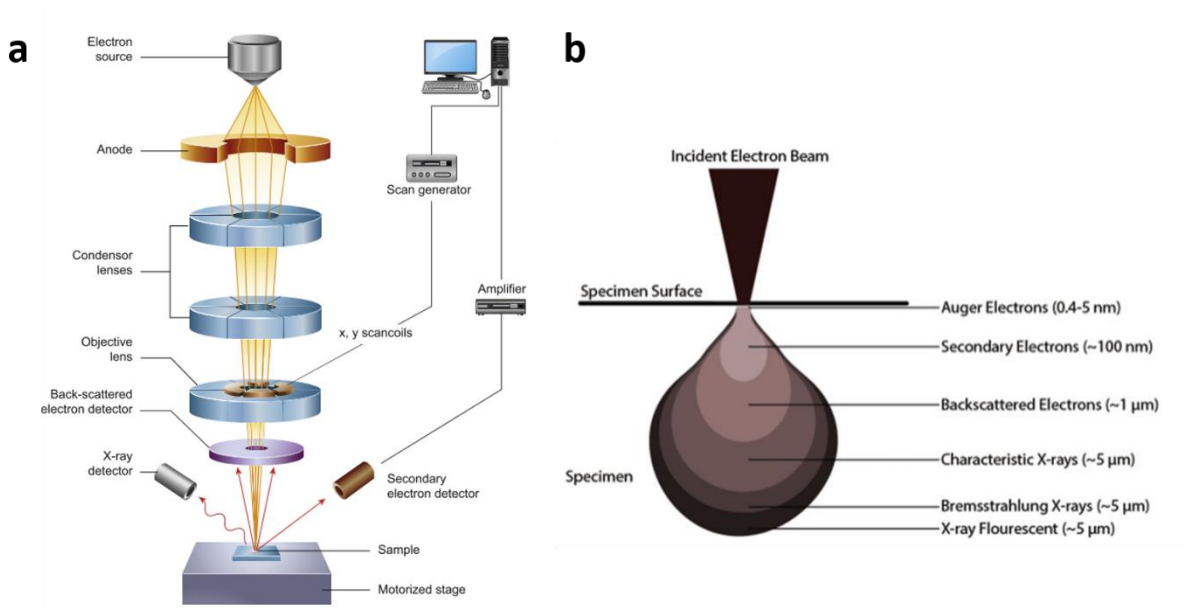

Figure 16. (a) schematics of the SEM instrument [41]; (b) different signals generated due to sample-electron beam interaction with different origination depths withing the excitation volume [40]

Fig 16b shows the different types of signal that are generated using SEM. The three mainly used signals are Secondary electrons (SE), backscattered electrons(BSE) and X-rays. These signals are used to generate information about the structure, molecular mass and chemical composition of the scanned surface, respectively.[40]

1. Secondary electrons (SE)

Once the incident beam interacts with the sample, the loosely bound valance electrons are ejected (fig 17a). These electrons usually have binding energies in the range 1-15 eV. SEs are known to have low kinetic energies since the energy transfer from the incident electron beam to the valence electrons is relatively small. Moreover, these electrons need to travel through the specimen experiencing inelastic scattering before reaching the surface further decreasing their kinetic energy. Because of this a significant portion of the SEs does not even make it out of the specimen.[39] The low ejection energy limits the depth from which the can be detected to a few nanometres below the scanning surface. It is noteworthy that the SEs are not solely limited to the ejected electrons that are kicked out by the primary electron beam. The BSEs, on their way out, can generate SEs as well. Which then would escape the surface at a point outside the electron beam, reducing the spatial resolution of SE imaging.[39]

2. Backscattered electrons (BSE)

Contrary to the SEs, backscattered electrons do not belong to the specimen under investigation. They are a fraction of the incident electron beam that interact with the positively charged atomic nuclei changing the direction of motion causing them to almost completely reverse their direction and return to the sample surface and subsequently leave it (fig. 17b). The energy level attributed to this class of electrons is usually between 50 eV and the energy of the incident beam (E_0).[41]

The significance of BSE lies within the fact that it generates atomic number contrast allowing to visually distinguish between different elements present in the specimen. The electric field around each nucleus which is responsible for the deflection and scattering of the incoming electron beam increases in strength with increasing atomic mass. Therefore, the deflection occurs more intensely resulting in a larger number of BSEs that can be ejected from the sample surface. Therefore, the areas containing higher atomic number elements appear brighter with higher gray levels in BSE image.[39]

3. Characteristic X-rays

When the ejected SE belongs to a shell other than the outermost shell of an atom, the vacancy can be filled by another electron from the next shell (fig. 17c). While dropping down to a lower energy level, this electron emits an x-ray with an energy equal to the energy difference between the two shells. This energy is unique for each atom and can therefore be used as a finger print to determine which elements are present in the specimen as well as their quantity.[39]

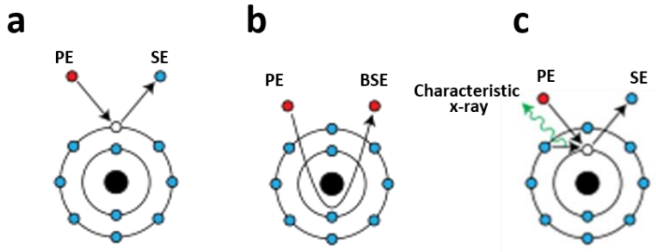

Figure 17. schematic representation of the underlying mechanism for generation of (a) SE, (b) BSE and (c) characteristic x-rays in SEM imaging. Image adapted from Wikipedia.org

Operating parameters

While making a SEM image there are several operating parameters the microscopist needs to control to optimize the image. When these parameters are not controlled optimally the image can appear blurry, information can be lost or at worst the sample can be damaged. Therefore a good understanding of these parameters is needed.

1. Beam energy

The energy of the incident electron beam has significant impact on several aspects of SEM imaging. To name a few, the size of the excitation volume, the intensity of the emitted x-rays, SE and BSE detection, charge build-up, beam damage, chromatic aberrations and extent of the resolved surface features are all directly dependent on the beam energy. Increasing the beam energy results in deeper penetration into the sample. Hence, lower beam energies are preferred for surface imaging at higher magnification and result in images with rich surface details. Moreover, lower beam energies make the results based on SE and BSE signals more comparable due to the similar volumes from which the electrons are originated.[39]

2. Beam current

Beam current is a measure of the number of electrons per second that the specimen surface is subjected to. The higher the beam current, the better the visibility of low contrast objects will be. However, a higher beam current also means a larger beam size which reduces resolution, not to mention increasing the probability of beam damage. Therefore, there is a limit to which one can increase the beam current. This limit is highly affected by the nature of the specimen under investigation and it's preparation. A typical beam current is about 1 nA, but beam currents in pA and μA range can be used as well. This is because a lower current density at a given beam energy, results in smaller prob sizes contributing to an increase in spatial resolution.[39]

3. Focus

In one sentence, bringing a beam into focus means that it will result in a sharp image that contains as much fine detail as possible. This is done by changing the focal length of the magnetic lenses. This is done by controlling the current going through the coils that form these lenses. The higher the current, the stronger the magnetic field and the shorter the focal distance of the lens will be. A shorter focal distance means a stronger convergence of the electron beam, decreasing the distance between the lens and the crossover point. The crossover point is the location where the beam is at is minimal diameter. Once this crossover point occurs on the surface of the sample, the beam will be properly focused.[39]

4. Working distance (WD)

The working distance is the distance between the pole pieces of the objective lens and the plane of best focus. A higher WD means smaller convergence angle for the incident beam resulting in the high depth of field mode in SEM imaging. However, the signal strength is decreased in this mode and the image may appear more noisy. On the other hand, using a low WD with a small probe size would improve the resolution, minimize the distance over which perturbations can occur and improve signal-to-noise ratio at the expense of losing depth of field.[40] Proper focusing of the beam results in the WD being equal to the focal length of the lens.

5. Astigmatism

Ideally, the cross section of the electron beam needs to be circular so that once the focus is adjusted, the beam reaches its narrowest mode and becomes a perfect geometrical point. However, in reality, imperfections such as lens aberrations do not allow this. For instance, the magnetic fields created in the lenses are never perfectly symmetric (usually stronger in one direction) which distorts the cross section of the electron beam from the ideal circle into an ellipse. Adjusting the stigmation is in fact trying to convert the beam cross section to a In the acquired image, this defect appears as stretches in one direction but not the other one, degrading the image resolution. Even though adjusting the focus of an astigmatic beam is able to reduce the effect, the obtained image will be inferior to the one acquired from focusing a well stigmated beam.[39]

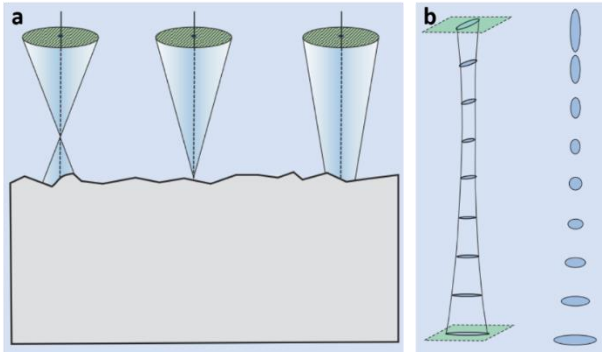

Figure 18. (a) schematics of the electron beam hitting the sample surface while overfocused (left), in focus (middle) and underfocused (right); (b) schematics of an astigmatic electron beam as it converges to focus and then diverges. The elliptical beam cross-section is least noticeable when it is in focus.[39]

Image defects

1. Charging

Studies have shown that only a fraction of the incident electron beam leaves the sample as SE or BSE. This means that in order to maintain neutrality, the rest of the electrons must leave the sample. If the electrons cannot leave, they will accumulate in the sample and result in the charging phenomenon. A charged specimen acts as a decelerator on the incoming beam, reducing the effective energy at which the beam reaches the surface. Therefor affecting the beam-sample interaction or, in extreme cases, acting like a mirror and deflecting the incident beam before it reaches the specimen surface. In the case of SEs, this charging usually results in acceleration of the SE leading to a much brighter and often saturated signal surrounded by a dark periphery that extends over the more conducting locations which collect the extra charge. This “false” brightness specially interferes with the interpretation of specimen topography where brighter areas are often perceived as edges and inclinations.

The flow of current to the ground from non-conducting samples is a major challenge in SEM imaging.[40] Almost all biological specimens are non-conducting once they are dried. This challenge can be overcome by means of a conductive coating layer. This coating increases the conductivity of the surface, decreasing the likelihood of charge accumulation. The ideal coating material is one which is featureless and can be deposited continuously. Since the coating is generally done from the top of the sample, the sides of the sample often do not receive much coating. This will interrupt the conducting path from the sample surface to the ground, negating the effect of the coating. Contact with the ground can be achieved by putting conductive materials, like silver paste, around the edges of thick samples.

2. Radiation damage

As the electrons land on the sample surface with high energies, the interaction taking place between the sample and the incoming beam might cause ionization, subsequent heat generation and chemical reaction. All of which will result in permanent damage to the sample. The extent of this damage varies in different samples, with soft materials and organic compounds being more susceptible since they are not considered good heat dissipators.[42]

Actions such as lowering the acceleration voltage, probe current and exposure time as well as applying an appropriate conductive coating would aid in reducing this irreversible damage. Presence of collapsed areas as well as horizontal lines parallel to the scanning direction of the sample surface are possible indication of beam damage.[39]

2.2 Transmission electron microscopy (TEM)

Transmission electron microscope (TEM) is an electron microscopy method applied to ultrathin sections. Even though both SEM and TEM use electrons for imaging, very different information is obtained from both techniques. While the image in SEM is formed from the fraction of the incident electron beam that returns from the sample surface, images acquired from TEM are based on the fraction of electrons that are transmitted through the sample. To ensure that a detectable amount of electrons is transmitted through the sample ultrathin sections of the sample as well as the higher energy of the incident electron beam (80-300 keV) are used.[43]

Fig 19a illustrates the schematics of the components of a TEM. Similar to SEM, the condenser lenses focus the incident electron beam. The objective lens positioned underneath the sample is responsible to focus the transmitted electrons which are subsequently magnified by the projector lenses to form the image on a viewing screen.

Figure 19b represents the different types of signals that are transmitted through the ultrathin sample. In regular TEM (bright-field mode) the contrast originates from the differences in thickness as well as atomic number of the elements present in the sample. Thicker areas and regions containing high atomic number elements will scatter the electron beam and inhibit the transmission resulting in darker areas in the image and vice versa.

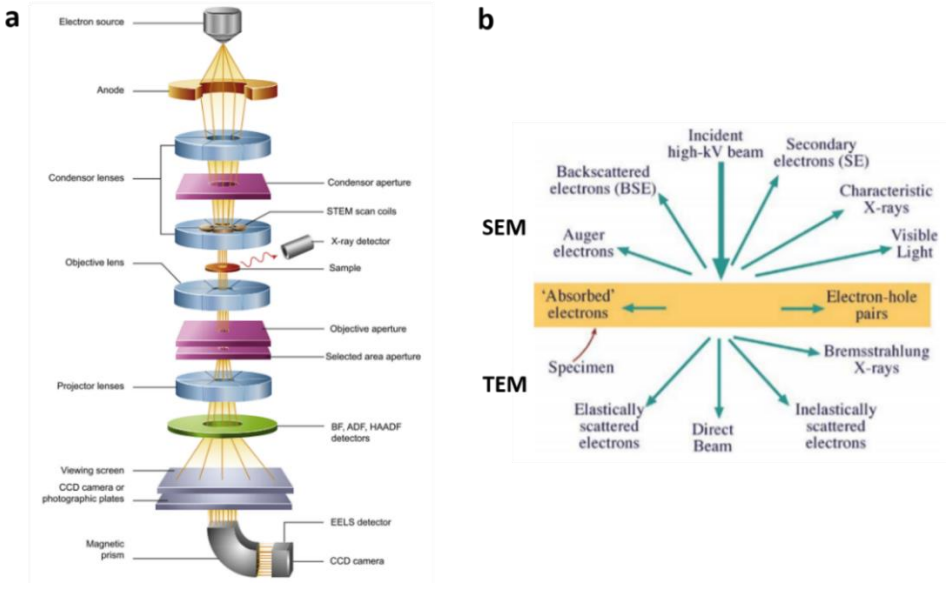

Figure 19. (a) schematic representation of the major components of a TEM [41]; (b) schematic representation of generated signals as the sample is exposed to a high energy electron beam [43].

2.3 Selected area electron diffraction (SAED)

SAED is a supplementary method often used in combination with TEM imaging to relate images to crystallography. The strong interaction of electrons with crystalline materials result in a predictable scattering and creates a specific diffraction pattern (DP). This DP is then used to determine the crystallographic orientation and lattice parameters of crystalline substances.[44]

The operating principle of SAED is that a selected area aperture is used to select a certain area of the specimen to form the DP. This aperture is usually inserted in the first image plane below the sample. Once an incoming parallel beam transmits through the sample, and the image is formed, the microscope is switched to diffraction mode where the focus of the projection lens is adjusted to coincide with the back focal plane of the objective lens and the DP is generated on the viewing screen. Fig 20a illustrates this principle schematically.[45] Depending on the nature of the crystal under investigation, DPs will have different shapes. A representative diffraction pattern for single crystalline, polycrystalline and amorphous materials is given in fig 19b. single crystalline materials have long range periodicity and their crystal lattice acts as a diffraction grate and creates single spots in the pattern. The SAED pattern of polycrystalline material appears as concentric rings. This is due to the fact that polycrystalline materials contain many single crystals that are randomly oriented and the DP is composed of the sum of DPs corresponding to each crystal. Amorphous material that contain no short range or long range periodicity, appear as diffuse rings in the DP.[46]

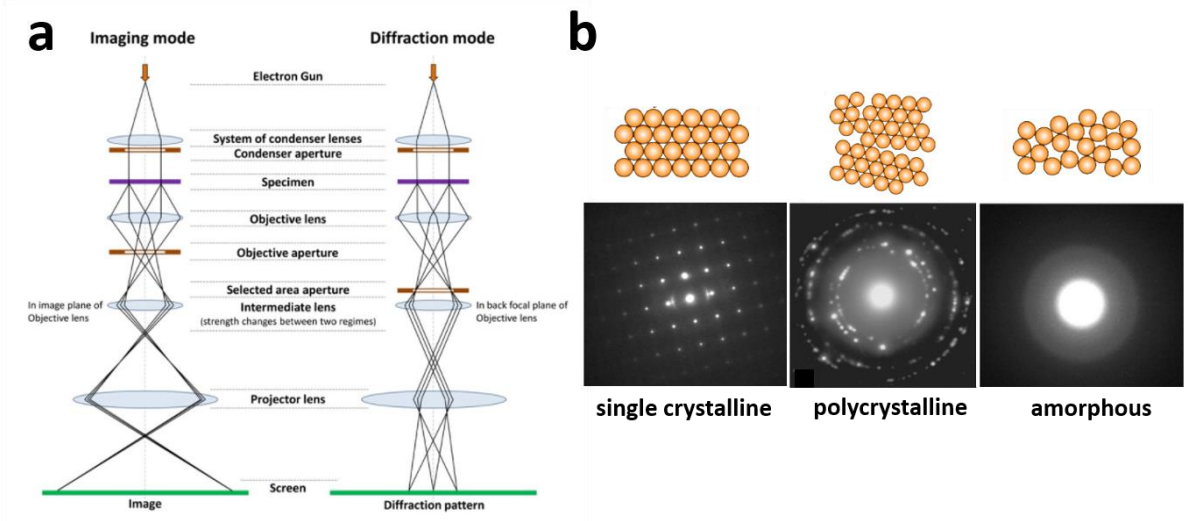

Figure 20. (a) schematics of a TEM equipped with SAED; image adapted from: Black Tubus (b) Diffraction patterns corresponding to single crystalline, polycrystalline and amorphous materials [46]

2.4 Cryogenic scanning electron microscopy (cryo-SEM)

Cryo-SEM is a mode of SEM which is effective in imaging beam-sensitive samples that contain moisture. It combines the high resolution imaging ability of regular SEM with cryogenic sample preparation methods. It is an appealing choice for studying biological specimens since it does not require sample preparation steps of regular SEM such as chemical fixation and drying and allows the investigation of the specimen in its native hydrated state. This fact makes cryo-SEM an excellent tool for studying the ultrastructure and morphological details of hydrated specimens. Furthermore, there is the possibility of freeze fracturing the specimen inside the cold chamber without exposing the specimen to external contaminants.[47] The samples are usually frozen using liquid nitrogen and are immediately transferred to the cryo-chamber in the frozen state and are maintained at low temperature inside the microscope chamber.[47]

2.5 Fourier transform infrared spectroscopy (FTIR)

Principle and instrumentation

FTIR is a vibrational spectroscopic method widely used for characterization of a vast range of materials and compounds. Infrared light interacts with a material in order to excite a vibrational state. A nonlinear molecule with N atoms that are covalently bound together, possesses 3N-6 vibrational modes. The vibrational modes that entail a change in the dipole moment of the molecule over the course of vibration are known as infrared active vibrational modes, meaning that they will absorb the incident infrared light. Consequently, a transition between quantized vibrational energy states occur, resulting in an absorption band in the infrared spectrum.[48] The energy difference between the ground vibrational state and the first excited state for most of the vibrational modes is in the mid-infrared region (400-4000 cm^{-1}). Functional groups have characteristic absorption bands corresponding to their fundamental vibrations which are used for their identification.[49]

The major component of FTIR is an optical device known as an interferometer (fig 21).[49] In this device, light from a broadband infrared source is divided by a beam splitter which is oriented at an angle of 45 with respect to the beam and results in production of two beams with equal intensity. Of these two beams, the transmitted one travels to a fixed mirror while the reflected one approaches a moving mirror. The returning beams from the two mirrors meet at the beam splitter and are recombined. This recombined beam is the one which will later on interact with the sample. Due to the difference in the length of their optical path which is caused by the distance between the moving mirror and the beam splitter, the reflected beams will undergo constructive or destructive interference upon merging in the beam splitter depending on the position of the moving mirror. This way, the beam will be modified to have all the different IR frequencies encoded into it since the periodic movement of the mirror would periodically block and transmit each wavelength.[50] Finally, the signal is decoded by Fourier transformation resulting in the FTIR spectrum.

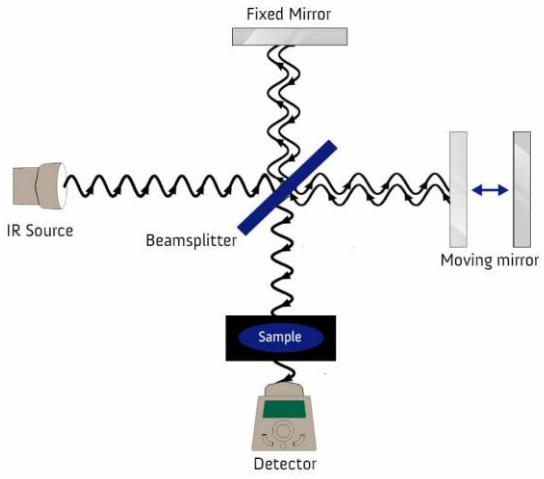

Figure 21. Schematic mechanism of FTIR. A monochromatic light beam is converted into a beam containing multiple frequencies through repeated constructive and destructive interferences which are created with the help of a beam splitter and two mirrors. The resulting light beam then interacts with the sample and the output is collected by the detector to form the FTIR spectrum. Image adopted from innovatechlabs

Attenuated total reflection FTIR (ATR-FTIR)

ATR is a variation of FTIR where the sample comes into contact with a sensing element. One advantage of this mode of FTIR is that the resulting spectrum is not due to transmission and thus, there is no need for very thin samples. Even for thick samples, the signal is gathered from the sample surface to a maximum thickness of about 2 μm. Furthermore, ATR allows us to analyze the solid samples directly without the need to alter it in any significant way such as reducing the thickness for transmission or mixing the sample with infrared transparent salts [51] which is conducive to our later investigation with SEM.

The sensing element (ATR crystal) is an optically dense crystal with high refractive index. Once the incident beam enters this crystal at a certain angle, internal reflections repeatedly occur. However, due to the contact between the sample and the crystal, after each reflection, a fraction of the reflected beam is absorbed by the sample resulting in the gradual attenuation of the internally reflected beam. This attenuating beam travels through the ATR crystal and is collected by the detector to form the interferogram and later on the FTIR spectrum.[52]

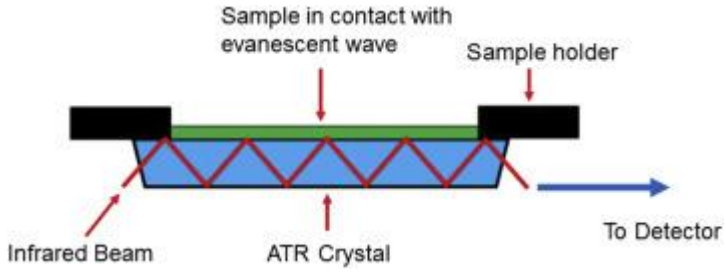

Figure 22. schematic representation for the working principle of ATR-FTIR; IR beam enters an optically dense crystal at a certain angle and is internally reflected. Prior to each reflection, a fraction of the beam is absorbed by the sample resulting in the attenuation of the reflected beam. The attenuated light exists the ATR crystal from the opposite end and is sent to the detector.[52]

ATR-FTIR spectrum of human bone

FTIR has a long history of application in bone research.[53] The nature of the components present in bone makes it an excellent sample for investigation with FTIR since each component (mainly collagen and carbonated HA) absorbs the infrared light at distinct regions in the IR (400-5000 cm^{-1}) range. Therefore, simultaneous information could be obtained on the organic and inorganic components. Moreover, it provides information on the state of the collagen as well as the phase of the mineral and possible crystal impurities such as carbonate and acid phosphates.

Fig 23 presents the FTIR spectrum of human cortical bone with the peaks which are assigned to significant vibrational modes in both the organic and inorganic phase. A summary of the peak assigned to each frequency are presented in table 1.

Table 1. Peaks assigned to different vibrational modes in natural human bone [54,55]

Wave number (cm^{-1})	Vibration mode	Wave number (cm^{-1})	Vibration mode
560-570	$v2\ PO_4^{3-}$	1100-1110	HPO_4^{2-}
600-613	$v_4\ PO_4^{3-}$	1410,1450	$v_3\ CO_3^{2-}(type\ B)$
860-871	$v_2\ CO_3^{2-}(type\ B)$	1566	$v_3\ CO_3^{2-}(type\ A)$
961-993	$v_1\ PO_4^{3-}$	1548	Amide II
1012,1036,1044,1092	$v_3\ PO_4^{3-}$	1634	Amide I

In this report we will focus on the vibrational modes of the inorganic phase. Among the main spectral bands for hydroxyapatite, the two bands around 557 and 600 cm^{-1} represent the $\nu_4\ PO_4^{3-}$ bending vibrations and the absorptions around 961 and 1014 cm^{-1} designate the symmetric and asymmetric stretching of $(\nu_1 + \nu_3)\ PO_4^{3-}$ respectively. The broad nature of the peak around 1014 originates from the poorly crystalline status of the apatite crystals in bone. It has been shown that the FTIR spectrum of a perfect stoichiometric HA crystal $[Ca_{10}(PO_4)_6(OH)_2]$ demonstrates an absorption band around 1030 cm^{-1}.[56] The mineral content of bone however, does not possess this perfection. The imperfection has been categorized depending on whether the phosphate (type B apatite) or hydroxyl group (type A apatite) has been replaced by anions such as carbonate and acidic phosphates. The mineral component of bone has been shown to be more of type B apatites.[57] The more intense absorptions at 1410 and 1450 cm^{-1} in fig 23 compared to the one around 1566 cm^{-1} as well as the well-resolved peak at 870 cm^{-1} are also in line with this statement. The sub-bands representing the vibrational modes of these substitutes, result in the aforementioned broadening of the $\nu_3\ PO_4^{3-}$ peak. Hence, dividing up this band into the underlying sub-bands via spectral deconvolution based on second derivative spectroscopy and curve fitting provides valuable information about the maturity of the crystals as well as the structure of the apatite crystals.[53]

In the initial stages of biomineralization, the nonstoichiometric apatites dominate. However, as the process continues, the mineral content displays less structural defects and the composition becomes more similar to that of the perfect hydroxyapatite. Conclusively, the shift in the center of the broad peak denoting the $\nu_3\ PO_4^{3-}$ could be an indication of the mineral crystals moving towards maturity and perfection.[58]

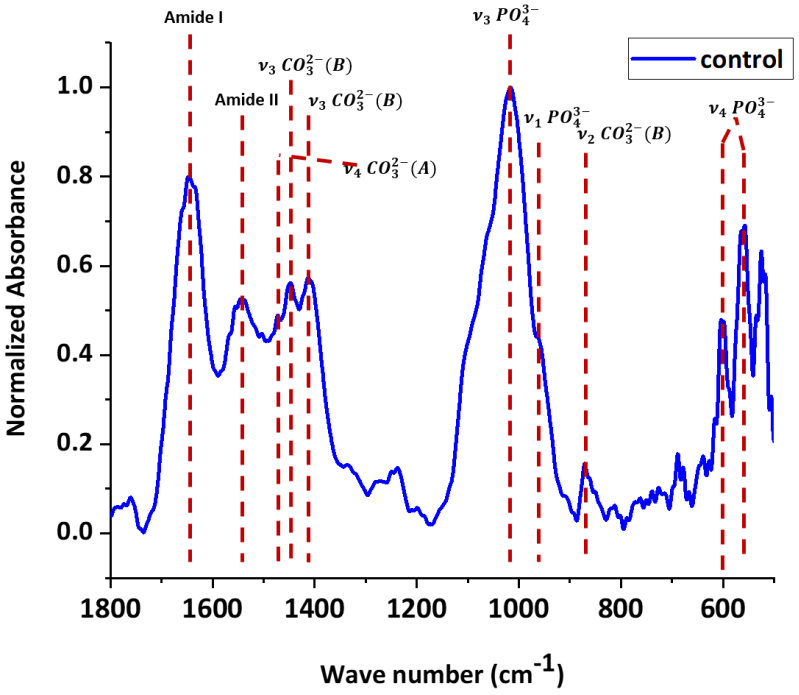

Figure 23. FTIR spectrum of human cortical bone in 500-1800 cm^{-1} range. The dashed red lines denote the frequency corresponding to different vibrational modes in both the organic phase (collagen) and the mineral phase (Hydroxyapatite). A and B in CO_3^{2-} refer to substitution of hydroxyl and phosphate groups in HA lattice respectively.

2.6 Inductively coupled plasma - optical emission spectrometry (ICP-OES)

ICP-OES is a technique that makes use of a plasma and a spectrometer to detect and quantify trace amounts of elements present in a solution. The plasma is generated from partially ionized Argon gas (typically less than 1% ionized in the plasma).[59] As a high frequency alternate current flows through an induction coil, an alternate magnetic field is created which accelerates electrons and sends them into a circular trajectory. Once these electrons collide with the Argon atoms, ionization occurs resulting in a stable plasma at the tip of a quartz torch.[60] The liquid sample is then drawn into the peristaltic pump and subsequently sent into a nebulizer where it is converted into a fine aerosol spray. In the spray chamber, larger droplets drain away while the finer droplet are directed towards the hot plasma. In the plasma, the aerosol vaporizes and its atoms get excited by having their electrons enter an excited "higher" state. Once this electrons fall back to their ground state, they emit a light characteristic to that specific atom. The light is then transferred to the high resolution optical system which separates the light into specific wavelengths. As these wavelengths strike the detector, light intensities for each different wavelength are quantified and finally, a software converts these intensities to concentration units.[61]

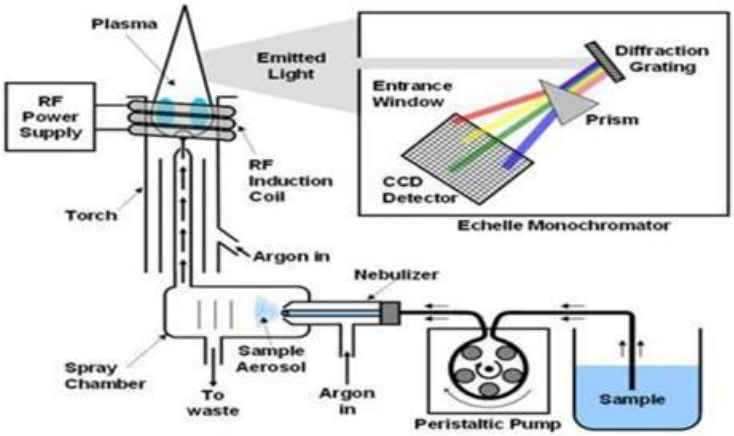

Figure 24. schematic representation of the working principle of ICP-OES. Image adapted from http://www.rohs-cmet.in/content/icp-oes

Chapter 3. Results and discussion

3.1 Deproteinization

Introduction

Investigating the morphology and structure of the organic phase has offered valuable insight into bone capability to function under unique mechanical demands. Similarly, isolating the mineral phase allows for study of the mechanical anisotropy of bone. This information could serve as a valuable reference for studying the nature of the defects in mineralization related diseases such as Osteogenesis Imperfecta and Osteoporosis. Moreover, due to the hybrid nature of the bone as a composite and the fundamental different interactions between an electron beam and organic and inorganic material, not all the details of bone as a whole composite could be resolved using electron microscopy.[13] However, by using a simple deproteinizing technique, it is possible to isolate the inorganic phase of bone and visualize it directly without any potential misinterpretations pertaining to the presence of the organic phase in electron microscopy images.[12] By applying this simple deproteinization technique, in this section we will investigate the bone mineral in terms of morphological evolution, orientation and structural integrity. This information will serve as reference for evaluation of the minerals created in vitro after remineralization of the organic matrix.

Treatment validation

Sodium hypochlorite (NaOCl) has been commonly used to remove the organic matrix of bone.[13,12,62] However it is still important to make sure that the treatment does not damage the mineral phase. To validate this, an FTIR spectrum of the treated bone was compared with that of the control and is presented in fig 25a. Absence of amide I (1640 cm^{-1}), amide II (1548 cm^{-1}) and amide III (1215 cm^{-1}) peaks proves the removal of the organic phase. Furthermore, we can clearly see the bands corresponding to different carbonate vibrations mainly around 870 and 1410 cm^{-1}. NaOCl has been reported to have the ability to dissolve the less mature mineral crystals of bone.[63] Hence, the presence of the carbonate bands in the FTIR spectrum could be considered as proof that even the imperfect carbonated HA minerals are still present after NaOCl treatment. A closer look at the $\nu_1, \nu_3\ PO_4^{3-}$ band between 900 and 1200 cm^{-1} illustrated in fig 25b also reveals a slight narrowing with less defined shoulders around the high wave number range (1050-1150 cm^{-1}). The smooth ascension towards the $\nu_3 PO_4^{3-}$ peak has been observed for pure carbonated hydroxyapatite.[55]

Comparing the SE images with the BSE images, we observe a strong correlation, providing us with evidence that we are observing only the mineral fraction of bone. Fig 25c shows a 55×38 μm area of the sample surface imaged in SE mode, accompanied by its BSE image in fig 25d. As we can see, both the SE and BSE image are in complete agreement with each other showing homogenous distribution of signal intensity. Providing further evidence of a single phase being present in the sample.

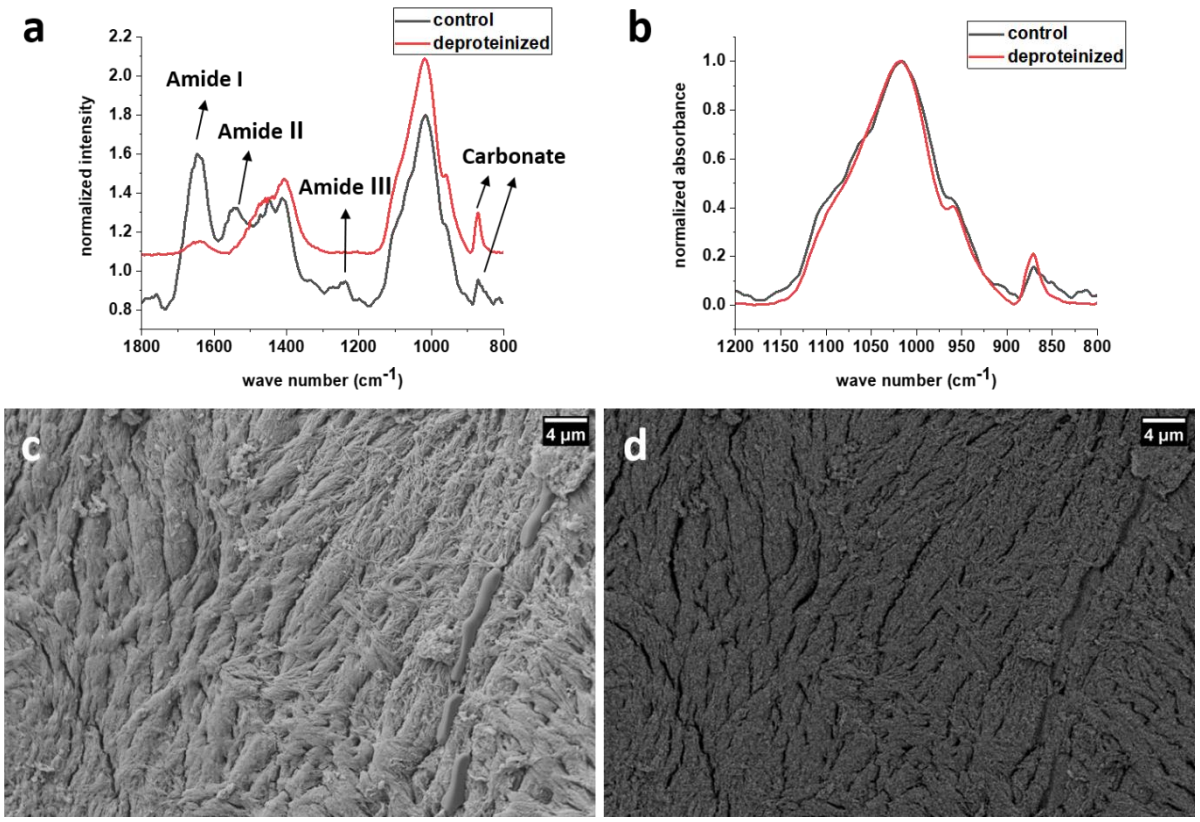

Figure 25. (a) FTIR spectra of natural bone (black curve) and deproteinized bone (red curve) displaying the absence of amide I (1640 cm^{-1}), amide II (1548 cm^{-1}) and amide III (1215 cm^{-1}) peaks, (b) Overlay of FTIR spectra between 800-1200 cm^{-1} ($\nu_1, \nu_3\ PO_4^{3-}$) ; No significant change or shift is observed in the shape of the $\nu_1, \nu_3\ PO_4^{3-}$ band and the $\nu_2 CO_3^{2-}$ peak at 870 cm^{-1} is retained indicating that the immature carbonated HA are still present after deproteinization, (c) an SEM image of the deproteinized sample with the corresponding BSE image (d) displaying equal spatial distribution of gray value intensities. The brightness and contrast of the BSE image are optimized using ImageJ for better visualization.

Morphological evolution

Resorption tracks that appear as pits in electron microscopy images could be caused by osteoclastic activity. These tracks are where the bone remodelling takes place and new bone apposition occurs Therefore, the different morphology of minerals inside and around these tracks could serve as a suitable road map for correlating the mineral shape with its age and maturity. Fig 26a shows the overview of an area where a resorption pit similar to what is described in [64] and [12] is visible. A magnified image at one end of this track is presented in fig 26b where the pit inside the track contains globular spherulites with 220-540 nm diameter which have been reported to be evidence of newly formed bone.[25,63] The existence of these calcospherulites is further proof that the deproteinization method and conditions have not been overly aggressive and have left these immature minerals intact.[63] Moving further down from these spherulites (fig 26c), we observe mineral platelets that are bundled up and have formed separate leaf-shaped discrete motifs which are about 0.6-3.6 μm long and 0.2-1.5 μm wide. Shah et al. have also reported the presence of these discrete leaf-shaped motifs in rat skulls close to the cranial sutures which are known to be primary sites for bone formation and have claimed these motifs to be a distinct stage of mineral maturation.[13] Moving further away from the resorption track (fig 26d) both the calcospherulites and the discrete leaf-shaped motifs gradually become less frequent, giving way to what seems to be a more mature and homogeneous form of mineral bundles. In fact, while the calcospherulites disappear, the discrete leaf-shaped bundles seem to coalesce and transform into more continuous structures. 3D electron tomography has shown a very similar description of collagen fibrils that are surrounded by mineral platelets in the form outlined by

the brown dashed-box.[23] Finally, the interwoven mineral bundles become the dominant morphology of the bone. Fig 26e illustrates this dominant morphology on a resting bone surface immediately outside the resorption track under investigation. A summary of morphological evolution is given in fig 26f.

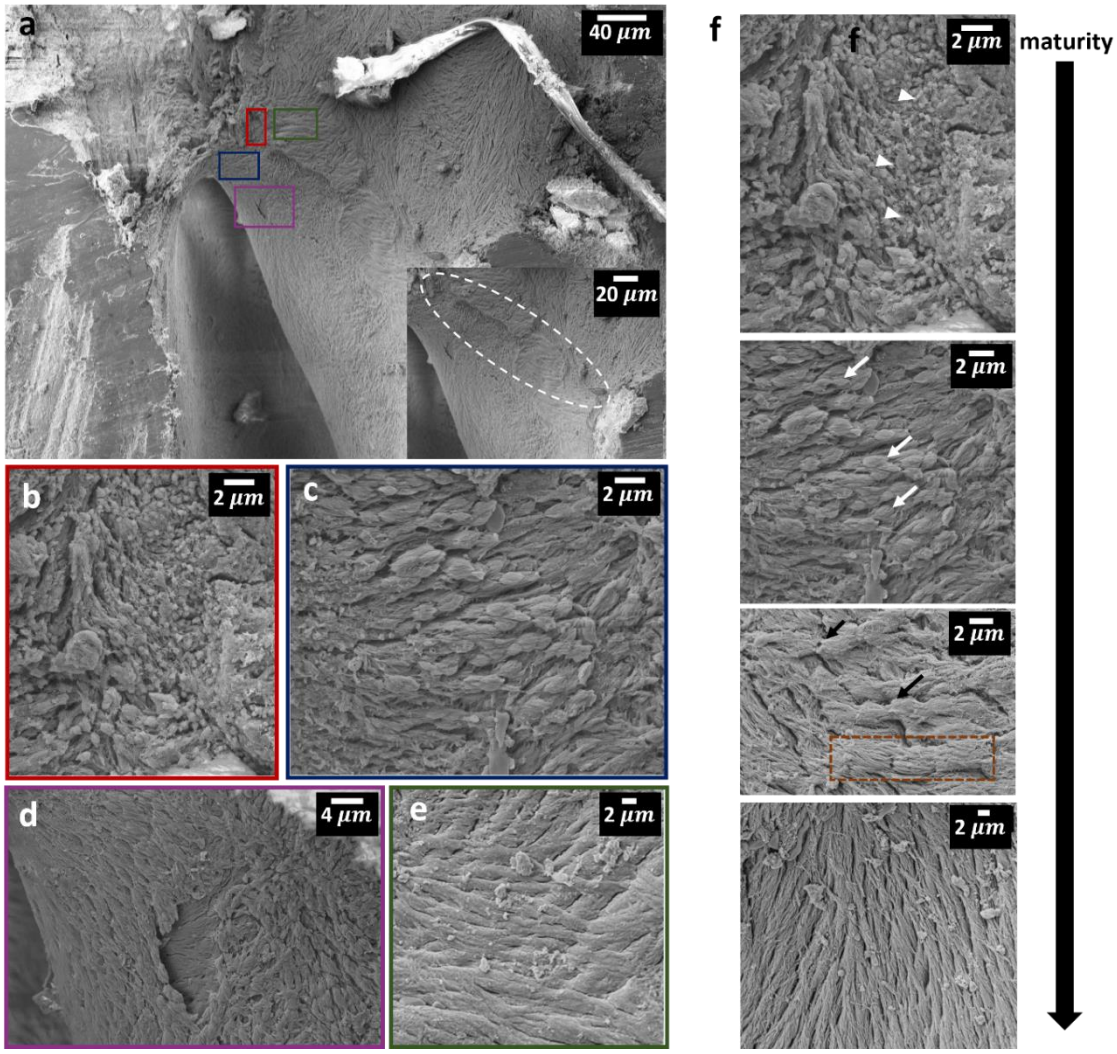

Figure 26. (a) overview of an area containing a resorption track with several areas (colored boxes) investigated inside and surrounding the track; the white dashed ellipse in the inset denotes the resorption track; (b)-(e) higher magnification of the areas noted in (a) displaying different morphologies of the mineral phase; (f) morphological evolution of the minerals in the following order: calcospherulites fusing into collagen fibrils (white arrow-heads), discrete leaf-shaped motifs (white arrows), fusion of the leaf-shaped motifs (black arrows) forming bundles of mineral platelets that are stacked laterally and tip-to-end (black arrow-head), and continuous bundles of platelets woven around each other in bundles that follow the direction of the removed collagen fibrils.

Even though these changes in morphology seem to occur gradually, some abrupt changes are also visible. The osteocyte lacuna in fig 27a displays edges that are comprised of the leaf-shaped motifs. Whereas, the floor of the lacuna is built up of aligned mineral platelets that are fused together. Similarly, the surface surrounding the lacunae in fig 27b includes both tiny calcospherulites and randomly dispersed needle-like minerals, while the floor of the lacuna exhibits minerals organized in bundles roughly following the direction of the lacuna long axis. This observation underlines the highly heterogeneous distribution of bone mineral in terms of maturity and emphasized the importance of other factors that play a role in the maturation of the mineral phase in bone such as proximity to the haversian canals, contact with the cells, etc.

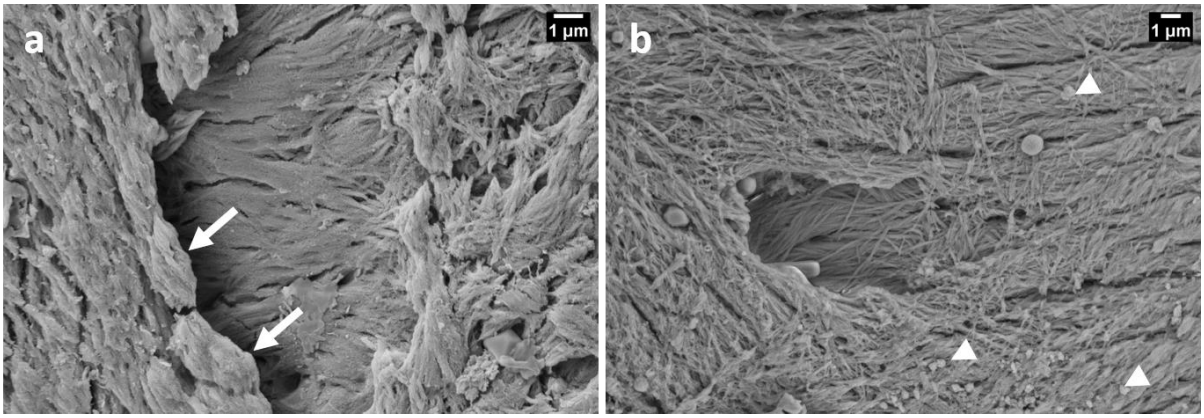

Figure 27. Morphological differences in the minerals residing in and around the osteocyte lacunae. (a) the edges surrounding the lacuna are made up of leaf-shaped motifs on the left and unorganized motifs on the right while the floor contains highly fused mineral bundles; (b) the surface surrounding the lacuna contains calcospherulites and randomly deposited platelets while the floor displays organized bundles.

Orientation and lamellar build-up

It has been reported that the osteocyte lacunae often stretch in the direction of the collagen fibres.[65] Therefore, the long diameter of a lacunae in each location could be a reliable indication of the orientation of collagen fibres in the same area. Fig 28a represents an osteocyte lacunae surrounded by 1-3 μm thick bundles of mineral platelets which follow the same direction as the long diameter of the lacunae. Each bundle is comprised of mineral platelets that are stacked both laterally and tip to end, weaving around each other. The dark spaces in between with 100-300 nm thickness could be the areas which used to be occupied by loosely mineralized or non-mineralized collagen fibrils. This coherency with the fibre dominant orientation could aid in understanding how the lamellar bone was built up. Since the sample under investigation was longitudinally cut, two successive layers of mineral bundles could be representative of adjacent lamella. Fig 28b displays what seems to be two successive layers, each with a different dominant direction. The angular difference between these visible dominant directions is in line with what *Reznikov et al.* describe regarding the make-up of the plywood-like structure of lamellar bone where they report a 45-80° angular offset between two adjacent layers of demineralized collagen.[18] Hence, with a simple deproteinization technique, it is possible to investigate the incremental build-up of the lamellar structure without the need for sequential sectioning.

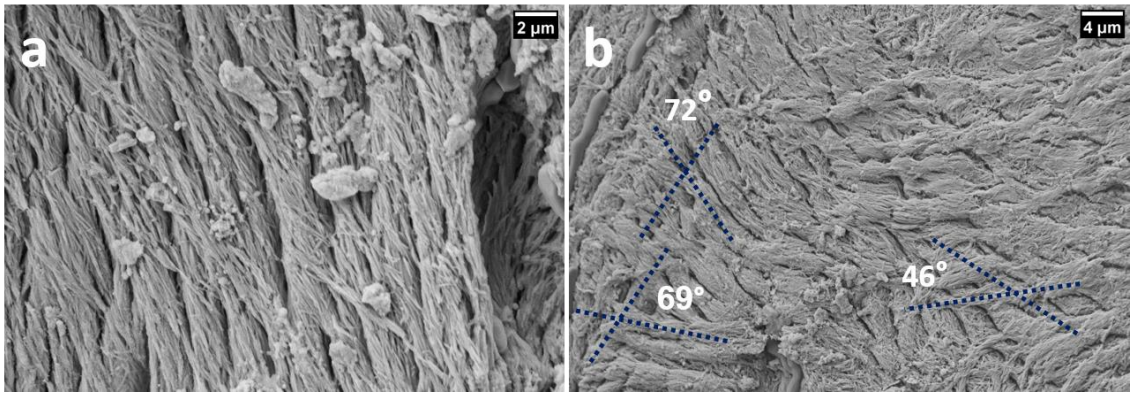

Figure 28. (a) an osteocyte lacuna stretched along the collagen fibril direction; the mineral bundles surrounding the lacuna follow the same direction; (b) mineral bundles in two adjacent layers displaying a 45-80° angular offset with respect to each other.

It is also noteworthy that even after the removal of the organic matrix and exposing the mineral phase to dehydration, drying and high vacuum inside the SEM chamber, the minerals still possess a high degree of structural integrity that enables even the earlier mentioned discrete motifs to stand alone without the support of the organic phase.

Conclusion

In this section, for the first time to our knowledge, the microstructure of the mineral phase in human cortical bone was investigated. We have used sodium hypochlorite to isolate the bone inorganic phase with the aim to better visualize the ultrastructure of the minerals. We have observed that at resorption tracks left behind by osteoclastic activity, bone apposition initiates in the form of small spherical particles with a diameter between 200-500 nm. These calcospherulites mark the most immature form of bone mineral phase. Gradually, collagen directed mineralization proceeds and the spherical minerals are replaced by mineral platelets that are organized into discrete leaf-shaped motifs which are later on bridged together to form continuous interwoven bundles along the long axis of collagen fibrils. These differences in morphology and maturity of the inorganic phase occur in a highly heterogeneous manner throughout the bone surface. Furthermore, the plywood-like structure of the lamellar bone can be observed based on the angular rotation in dominant direction of two successive layers of minerals. The clear microstructure and organization of the inorganic phase and its structural integrity after the removal of the organic phase, undoubtedly has significant contribution to the unique mechanical characteristics of bone and needs to be paid attention to, while studying the remineralization of the bone organic matrix in vitro. Furthermore, the structural model we have proposed here for the microstructure of the mineral phase, could provide a valuable reference for studying the malfunction of bone biomechanics in mineralization-related diseases.

3.2 In-vitro re-mineralization of human cortical bone

3.2.1 Demineralization

Introduction

For many research and clinical purposes bone tissue needs to be demineralized before analysis. The two main methods used are the use of acidic solutions and the use of chelating agents. Each of these methods have different effects on the structure and chemistry of the tissue. Therefore the demineralization process should be optimized for each individual research purpose with care so as not to negatively affect the results of the subsequent experiments.

In this research the complete demineralization of the specimens was required, as not to interfere with the in vitro mineralization. As specified before, it has to be validated that the demineralization process does not affect the bone structure and chemistry, since this could negatively impact the in vitro mineralization. That being said, the time required for the reaction needs to be monitored as well, in order to ensure that the process is not needlessly time-consuming.

Acidic agents such as hydrochloric acid (HCl) and nitric acid (HNO_3) reserve the advantage of achieving the desired level of demineralization in a short amount of time. However, this rapid decalcification comes with the risk of morphological destruction and loss of antigenicity for the tissue.[66] Chelating agents on the other hand are able to remove the mineral content of the bone while preserving the structure, with the drawback of a longer required processing time.

In the following, we show the optimization of the demineralization process in terms of temperature, duration and concentration of the decalcification agent. EDTA was chosen as the demineralization agent. First, two different concentrations of EDTA were chosen for the experiment at room temperature. This was done to study the effect of concentration on the extent of calcium removal via ICP-OES. Once the proper concentration was determined, the duration for adequate demineralization was studied with the chosen concentration at 4°C. Finally, the desired end-result of the demineralization process was validated by other characterization techniques namely, FTIR and SEM and the ultrastructure of the organic matrix was investigated.

Dynamics of demineralization

Fig 29 shows the x-ray images for demineralization experiments done in 25°C with (a) 5% EDTA and (b) 9.5% EDTA for a period of 7 days. The gray value intensity of the tweezers is used as a reference.

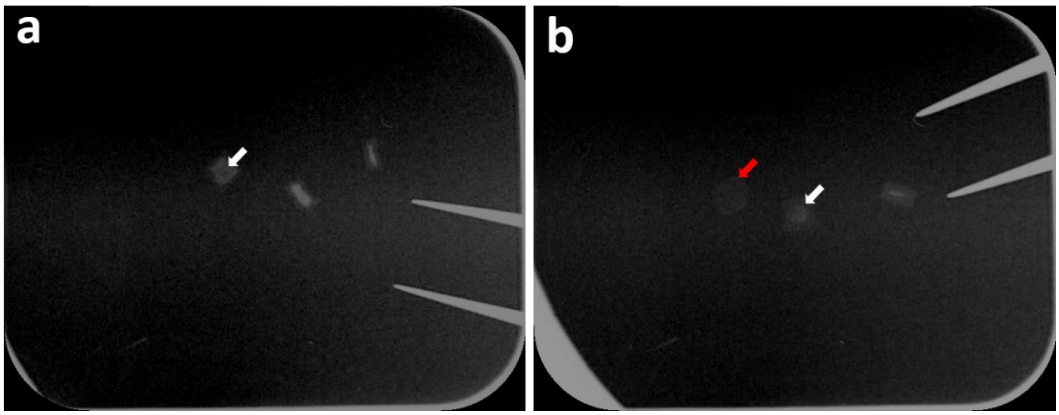

Figure 29. x-ray images showing bone blocks demineralized with (a) 5% EDTA and (b) 9.5% EDTA in 25°C. The white arrows point to the mineral content in the core of the blocks. The red arrow points to an almost completely demineralized block.

The diffusion limitation of the demineralization solution is evident in these images. The core region of the blocks shows higher intensity indicating high mineral content in both concentrations, while the regions close to the surface display a faint signal indicating higher percentage of mineral removal. Furthermore, observing the extent of bright regions in the blocks, after 7 days of demineralization, use of 5% EDTA depicts significantly less demineralization compared to 9.5% EDTA. In fact in fig 29b, the block on the left (red arrow) shows nothing but a faint shadow, indicating the near total removal of the inorganic phase.

These observations were confirmed quantitatively with ICP-OES measurements. Table 1 (supplementary information) displays the concentration of Ca^{2+} ions in ppm (parts per million) as the output of the measurement as well as its equivalent mg per 10 ml of each solution. The samples weighed 41.50 and 47.00 mg for 5% and 9.5% EDTA, respectively. This leads to a total respective amount of 10.81 and 12.24 mg calcium content. For the gap between days 4 and 7, the amount of calcium detected for the whole period was divided into equal amounts for each day within the time interval.

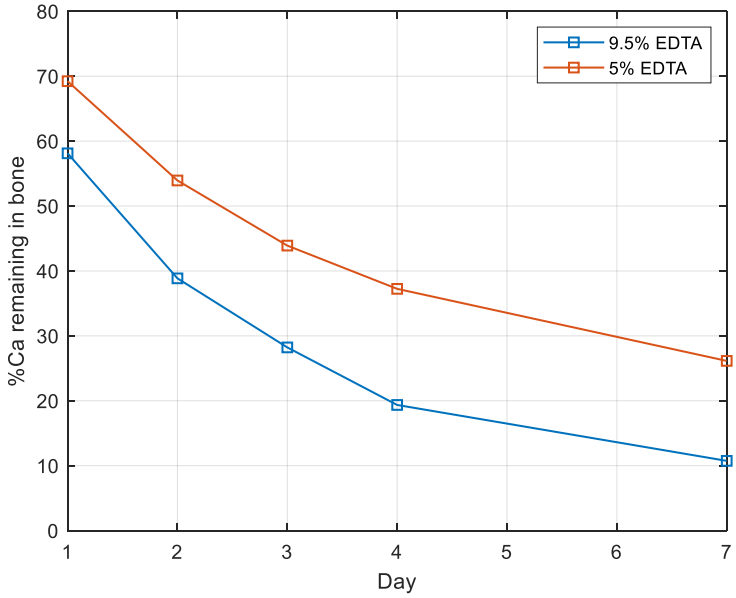

Figure 30. ICP-OES measurements showing percentage of calcium left in bone for demineralization using 5% and 9.5% EDTA at 25°C for a period of 7 days.

The progression of calcium removal is shown in fig 30. As we can see, the largest drop in the calcium content of the samples, belongs to the first 24 hours during which the surface of the samples are mostly being demineralized with little diffusion effects to hinder the process. In fact using 9.5% EDTA, almost 42% of the total calcium content of the sample is removed during the first day which accounts for almost half of the total removal achieved at the end of the process. However, as the demineralization extends towards the core, the slope of the lines between each 2 consecutive time points is reduced indicating that the demineralization solution faces difficulty diffusing through the block. In the end, after 7 days, a total amount of 73.85% and 89.26% calcium removal was achieved for 5% and 9.5% EDTA respectively at room temperature.

5% EDTA resulted in 73.8% calcium removal after 7 days. Moreover, during the last day of the experiment, we only achieved 2.87% of calcium removal. We also anticipated that the difficulty of

having the demineralization solution diffuse through the sample would result in further drop in the removal rate for an extended period of the experiment. Therefore, we concluded that 5% EDTA is too gentle of an approach for our research purposes and the time required to achieve complete demineralization with this concentration would not be practical.

Meanwhile, 9.5% EDTA actually results in a high degree of demineralization after 7 days with only 10.7% of the mineral phase left in the samples. Therefore, the next experiment was conducted with the same specifications but this time for 12 days with the aim of achieving full demineralization as well as at 4°C to better protect the structure of the organic matrix while comparing the results with that of the one done in 25°C.

Similar to the previous experiment, first a x-ray image was taken from the demineralized samples which is depicted in fig 31. The rectangular areas marked by the white arrows only display a faint shade left of the samples representing the organic phase and no proof of mineral presence is evident in the image.

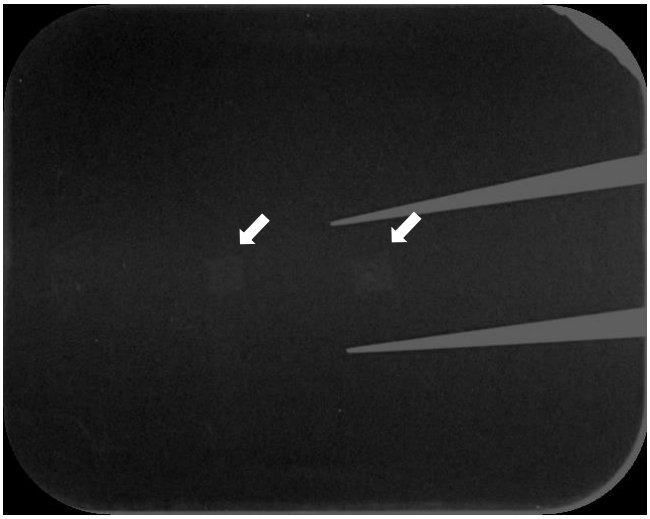

Figure 31. X-ray images showing bone blocks demineralized with 9.5% EDTA for 12 days at 4°C

Table 2 (supplementary information) shows the ICP results for 12 day demineralization using 9.5% EDTA at 4°C. The samples weighed 33.31 mg which leads to a total amount of 8.67 mg calcium content. For the gaps between days 2 and 5 as well as days 8 and 12, the amount of calcium detected for the whole period was divided into equal amounts for each day within the time interval.

The results state that after 12 days, more than 99% of the total calcium content of the bone samples was removed bringing them very close to total demineralization. The remaining calcium content after each time point is illustrated in fig 32a.

While we established the appropriate duration for total demineralization using 9.5% EDTA, it was also noteworthy to make a comparison between the removal percentages that occur at 4°C and 25°C with the same concentration of EDTA. Fig 32b displays the amounts of removed calcium per day at each temperature. As anticipated, higher temperature results in more calcium removal. Nevertheless, we are able to achieve complete demineralization after 12 days. Considering the fact that lower temperatures are far more effective in preserving enzyme reactivity of the tissue.[66] For the purpose of this research, 4°C is the suitable choice.

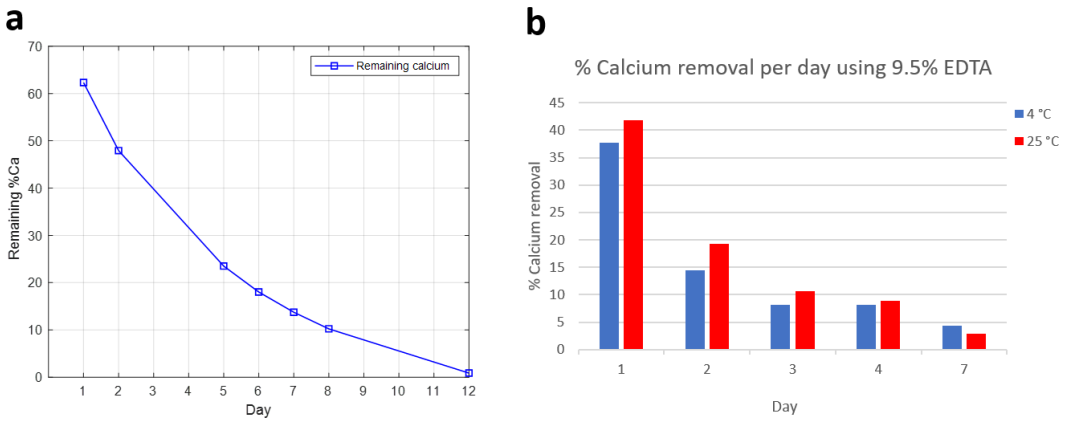

Figure 32. (a) ICP-OES measurements showing percentage of calcium left in bone for 12-day demineralization using 9.5% EDTA at 25°C. (b) Comparison between daily calcium removal rate at 25°C and 4°C using 9.5% EDTA.

In smaller samples, it is easier to prevent loss of enzymes, antigens and proteoglycan content during fixation and demineralization.[66] They also require less time for complete demineralization. Moreover, thinner samples are less susceptible to charging artefacts during SEM investigation since the incoming electrons will more easily travel through the sample towards the conductive carbon tape and thus get trapped less often. Considering the fact that charging is one of the main challenges in the way of reliable image acquisition in SEM investigations, using thinner samples would provide us with more time to effectively investigate an area before charging can compromise the obtained results. Hence, from here onward, all the samples under investigation were prepared in 100 μm thin sections using a vibratome. Moreover, demineralization of the blocks with 1 mm thickness required 12 days. The prepared slices are 10 times thinner. Therefore, a practical yet reasonable choice of 5 days was deemed appropriate for ensuring complete demineralization of the slices.

In order to validate the results obtained from chemical analysis of the demineralization solution, ATR-FTIR was used to determine the IR spectrum and thereby confirm the bulk demineralization of the bone slices.. The results are illustrated in fig 33a. As a reference, the IR spectrum of collagen type I obtained from pure (dry) membranes of bovine Achilles deep tendon is given in fig 33b.[67]

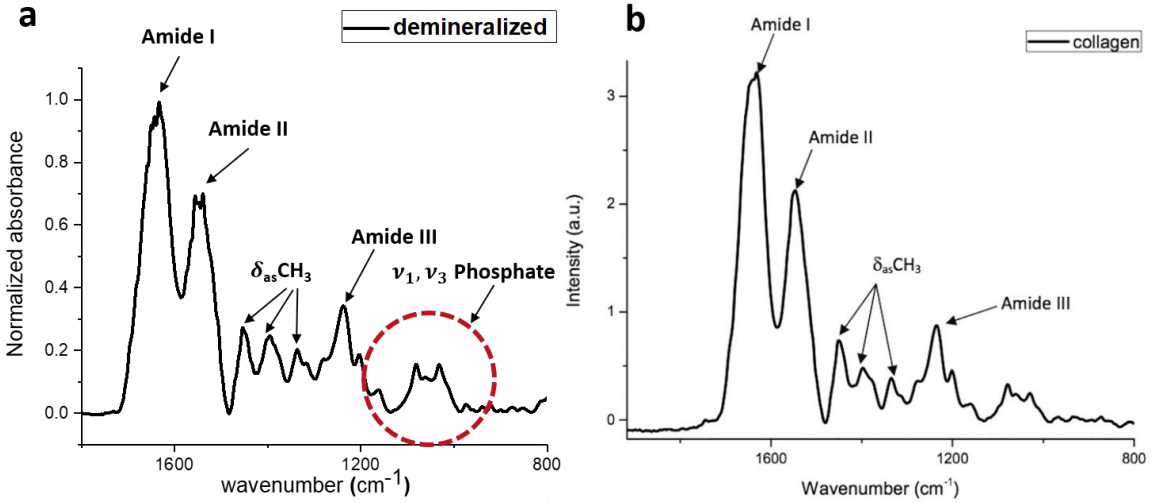

Figure 33. (a) FTIR spectrum of human cortical bone demineralized for 5 days. The area outlined by the dashed circle denotes the 900-1200 cm^{-1} area where the phosphate bands are absent. (b) IR spectrum of collagen type I obtained from pure (dry) membranes of bovine Achilles deep tendon.[67]

The two figures look very similar in terms of the peaks associated with amide bonds. The absence of the broad shouldered peak between 900 and 1200 cm^{-1} designating the phosphate bonds is also proof of the decalcified nature of the sample under investigation. The twin peaks at 1032 and 1080 cm^{-1} correspond to C-O, C-C stretching vibration and to C-O-H and C-C-O bending vibrations respectively and thus are not a sign of mineral presence.[68]

Ultrastructure of demineralized bone

Fig 34a illustrates the ultrastructure of the demineralized bone. The repetitive plywood-like structure of the lamellar bone as described by Reznikov et al. can be clearly seen.[18] Bundles of collagen fibrils gradually change direction with reportedly 45-80° angular difference between adjacent layers[18] leading to regions with collagen fibrils lying in plane of the image (black arrow-head) as well as regions where the fibrils are sticking out with their tips pointing upward out of the image plane (black asterisk). The region marked by the red box is shown in higher magnification in fig 34c. In addition to the ordered bundles of collagen fibrils perpendicular and parallel to the image plane, the region in between (white arrowheads) is filled with loosely packed and randomly oriented collagen fibrils with dark areas in between them. While the fibrils in the ordered and aligned regions are densely packed with negligible pores in between them, our observations were in agreement with those of *Reznikov et al.* who have described the disordered areas as regions containing most of the sub-micron pores of the bone.[18] Fig 34b demonstrates the backscattered electron image (BSE) of the same area depicted in fig 34a. The images overlay completely, with the backscattered image having a rather homogeneous gray scale intensity distribution after applying a median filter with a radius 2.0 indicating that the sample under investigation is homogeneous in composition (proteins, mostly collagen type I). The histogram for this image is given in fig 34d featuring a narrow bell-shaped peak spread across a narrow range of gray values. As a reference, a histogram representing the natural bone is also given which shows a broader peak with a shoulder at the same gray value where the demineralized bone displays its peak.

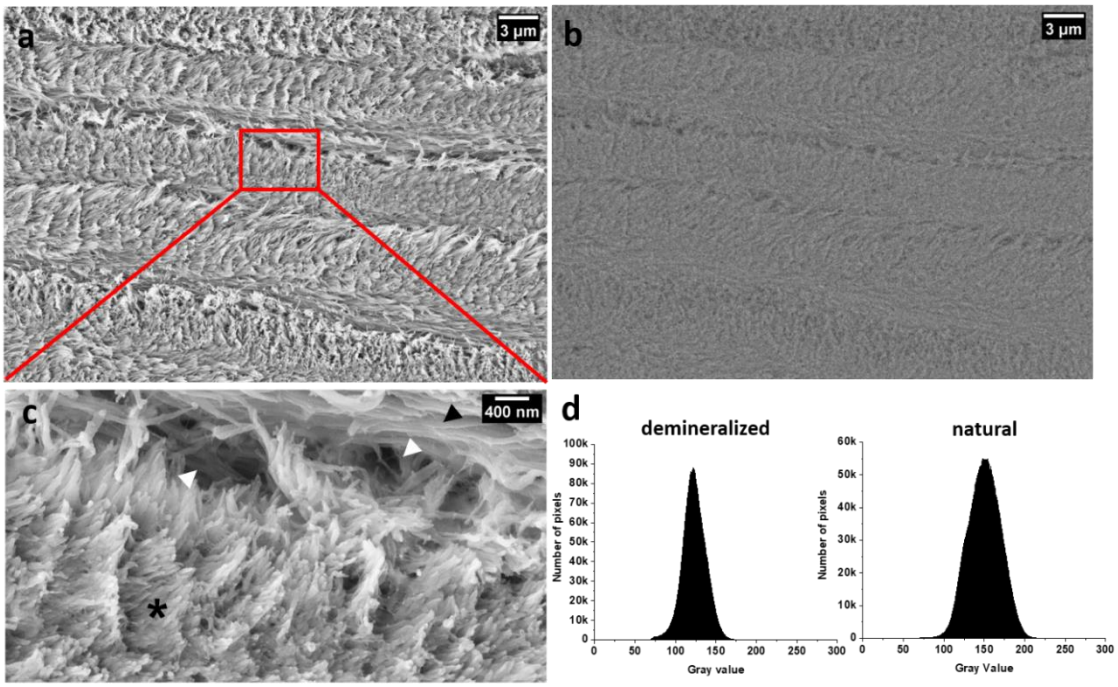

Figure 34. SEM micrograph displaying the ultrastructure of demineralized human cortical bone in (a) SE and (b) BSE mode. (c) higher magnification of the area outlined by the red box showing ordered bundles of collagen fibrils perpendicular (asterisk) and parallel (black arrow-head) to the image plane. White arrow-heads denote the region in between filled with loosely packed and randomly oriented collagen fibrils. (d) Left: gray value distribution of (b);right: gray value distribution of natural bone.

Fig 35 displays the ultrastructure of the collagen fibrils in an area where the bundles lie in the plane of the image. The banding pattern of collagen is evident in figs 35b. Rotating fig 35b clockwise for 9° and using the “plot profile” tool in Fiji for the marked fibril, the distribution depicted in fig 35c was obtained. The periodicity of the change in the intensity of the gray values as a function of distance is evident. However, the distance by which this periodic pattern repeats itself was determined to be approximately 56-58 nm. Considering the fact that the characteristic banding pattern periodicity of collagen fibrils is 67 nm, this difference could be the result of two assumptions based on which the plot in fig 35c was made: 1) The sample surface is assumed to be completely flat which probably is not the case here. This leads to the tilting of the fibrils upwards or downwards which in turn makes the periodicity calculated from the aforementioned plot, shorter than what it actually is. Furthermore, the fibril under investigation is assumed to be completely horizontal for the analysis which is not precisely true. 2) Demineralized collagen fibrils are greatly affected by the drying process which leads to their shrinkage. This could also be one of the main reasons behind the discrepancy we observe in the measured and actual periodicity of the banding pattern.

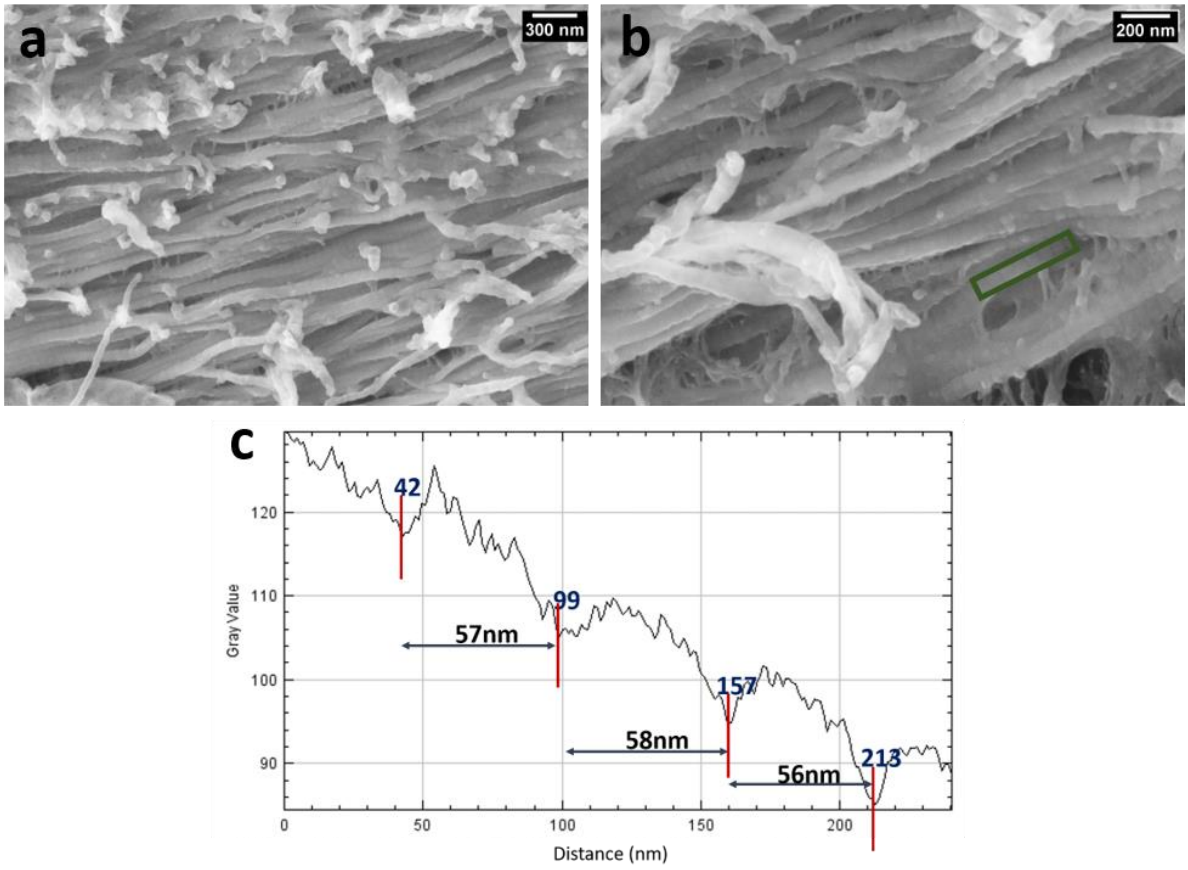

Figure 35. SEM micrographs of Low (a) and high (b) magnifications of demineralized collagen fibrils. (c) plot profile of the fibril inside the green box displaying the periodicity of the banding pattern.

3.2.2 Remineralization of collagen fibrils on a TEM grid

An important aspect in successful replication of biomineralization of the bone matrix is to create HA crystals which are aligned with their c-axis parallel to the direction of their supporting collagen fibrils.

In order to determine the orientation and phase of the created calcium phosphate minerals, ultra-thin sections of demineralized bone matrix with a thickness of 210nm were remineralized on a TEM grid. Use of ultra-thin sections for remineralization also has the advantage of minimizing the diffusion effects avoiding further complication of the remineralization process.[36] Fig 36a and 36b show bright-field TEM images of a demineralized section and a section remineralized for 2 hours, respectively.

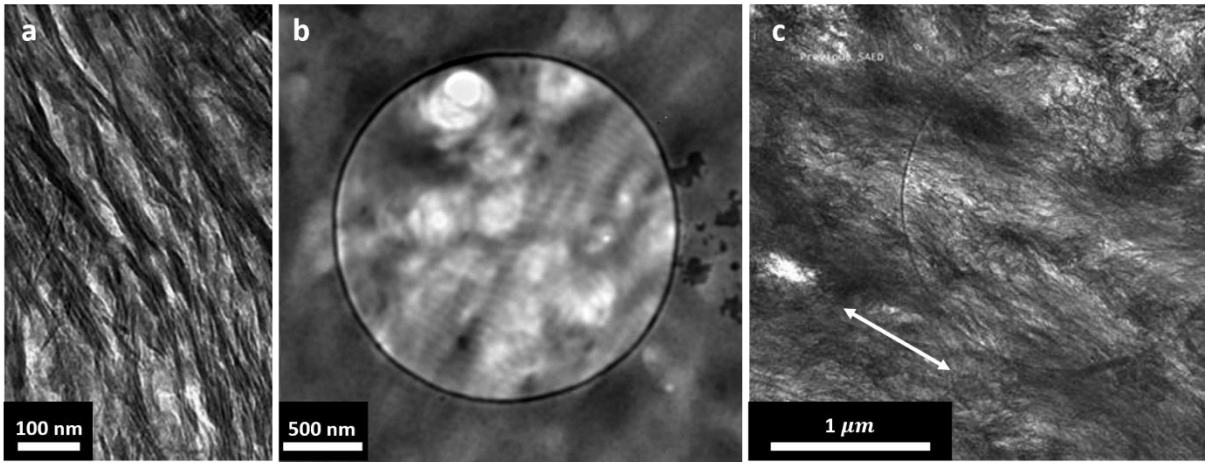

Figure 36. Bright-filed TEM images of (a) natural human bone [22], (b) demineralized bone matrix and (c) organic bone matrix remineralized for 2h. The double-headed white arrow indicates the general direction of the collagen fibrils.

The evident banding pattern of the collagen fibrils in fig 36b was determined to be 64 nm using FFT filtering. This banding pattern in fibrils with a diameter of about 80 nm validates the demineralized nature of the bone matrix prior to remineralization. After 2 hours of mineralization, the sample appears heavily mineralized. The banding pattern is barely visible and the presence of the minerals in some regions has completely blocked the outline of the grid holes.

The general direction of collagen fibrils appears to be in the direction defined by the white arrow in fig 36c. However, the extent of mineralization makes it difficult to make any statements regarding the collagen-mineral relation solely based on this image. Therefore, a selected area electron diffraction (SAED) was performed on the image in fig 36c in order to determine both the phase and orientation of the created minerals. The diffraction pattern is presented in fig 37a. The distinct two arcs are positioned 5.742 nm^{-1} apart from each other which translates into a d-spacing of 3.483Å consistent with the (002) plane reflection of hydroxyapatite. The more diffuse ring surrounding the two arcs has a diameter of 7.032 nm^{-1} which is translated into a d-spacing of 2.844Å consistent with the closely spaced (211), (112) and (300) planes of hydroxyapatite, further proving this phase to be the dominant phase of the created minerals [HA-JCPDS-09-432]. The gray value profile of the SAED pattern is given in fig 37c. The pattern was first rotated -23° using FIJI and a horizontal rectangular area was selected to make the profile. The peaks representing the middle points of the arcs were chosen for making the calculations. Moreover, the (002) plane is parallel to the c-axis of HA crystals. Therefore, the positioning of the two arcs representing this plane's reflection indicates a preferred orientation of the HA c-axis in the direction shown by the double-headed white arrow which is comparable to the direction determined for collagen fibrils in the corresponding TEM image.[69] A representitive SEAD pattern of human cortical bone is displayed in fig 37b for the sake of comparison.[70] This SEAD pattern

is reported to have a d-spacing of 3.474Å. As it is evident, the two diffraction patterns look very much similar further corroborating the successful replication of mineralization of the collagen fibrils in vitro.

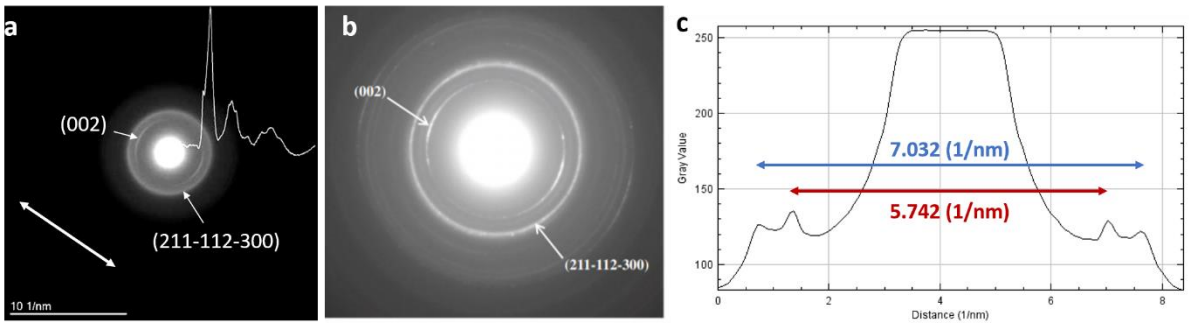

Figure 37. (a) SAED pattern of the BF-TEM image in fig 36(c); The two distinct arcs are reflection of the (002) plane in HA crystal lattice which is normal to the HA c-axis. Therefore the double-headed white arrow represents the HA c-axis direction which is along the dominant direction of collagen fibrils. (b) SAED pattern of a cortical mature bone displaying a d-spacing of 3.474 Å [70]; (c) Gray value profile of the SAED pattern in 2(a)

3.2.3 Bulk remineralization of dense collagen substrate

In the previous section, we showed that the biomineralization of collagen fibrils in human bone could be replicated in-vitro on ultra-thin sections.[36] In this section, we aim to take it one step further and study the bulk mineralization of the dense collagen substrate. To do this, we used the same composition of mineralization solution described before to mineralize 100 μm thick sections. The sections were cut out of cortical bone blocks using a vibratome.

As a starting point, we let the mineralization proceed for 1 day and 6 days with the general aim of detecting mineralization based on the backscattered (BSE) images.

<u>1-day mineralization</u>

Fig 38a displays an overview of the sample. Based on this overview, it appears that the top and bottom edges of the sample have been mineralized. However, at this magnification, the middle area does not display any indication of the presence of mineral phase. The three areas outlined by the coloured boxes were chosen for closer inspection. Fig 38b represents the osteon located in the middle section of the sample surface. The concentric circles around the osteon are the successive lamella each with a different dominant orientation of collagen fibrils.[6] A remarkable observation in this area was the loss of microstructure in some of the lamella that contained collagen fibrils normal to the imaging plane. This occurrence is possibly an artefact of cutting. As it is depicted in more detail in fig 38c, while the vibratome blade seems to have only scraped over the collagen fibrils lying within the image plane, the tips of the fibrils facing outward of the plane seem to have been fused together as the blade has moved through. At first, it was thought that this fusion could be due to the mineral phase which has filled the gap in between the fibril tips. However, the BSE image depicted in fig 38d proved no significant difference between the fused and non-fused regions. The BSE image displays very low intensities in very small areas which correspond to the presence of the small crystal precipitates. The absence of signal in the remaining pixels of the BSE image indicates that the majority of the collagen matrix in this region has remained non-mineralized.

Despite the middle area displaying little to no mineralization, the regions in the proximity of northern and southern edges appear mineralized. A closer look at the southern region is given in fig 38(e-f) and were similar to the mid-section, where an osteon is located. Contrary to fig 38c, the concentric lamella show a significant amount of mineralization. The collagen fibrils with their tips pointing out of the imaging plane seem to possess a higher degree of mineralization compared to the fibrils lying in plane,

possibly due to higher exposure of these fibrils to the mineralization solution. Cutting artefacts are again evident at the upper right edge. Finally, the interface between the mineralized and non-mineralized area at the northern edge is given in fig 38(g-h). We clearly observe a continuous mineralization front that has started from the edge and stopped towards the center with localized nucleation sites which happen to be located inside the lacunae.

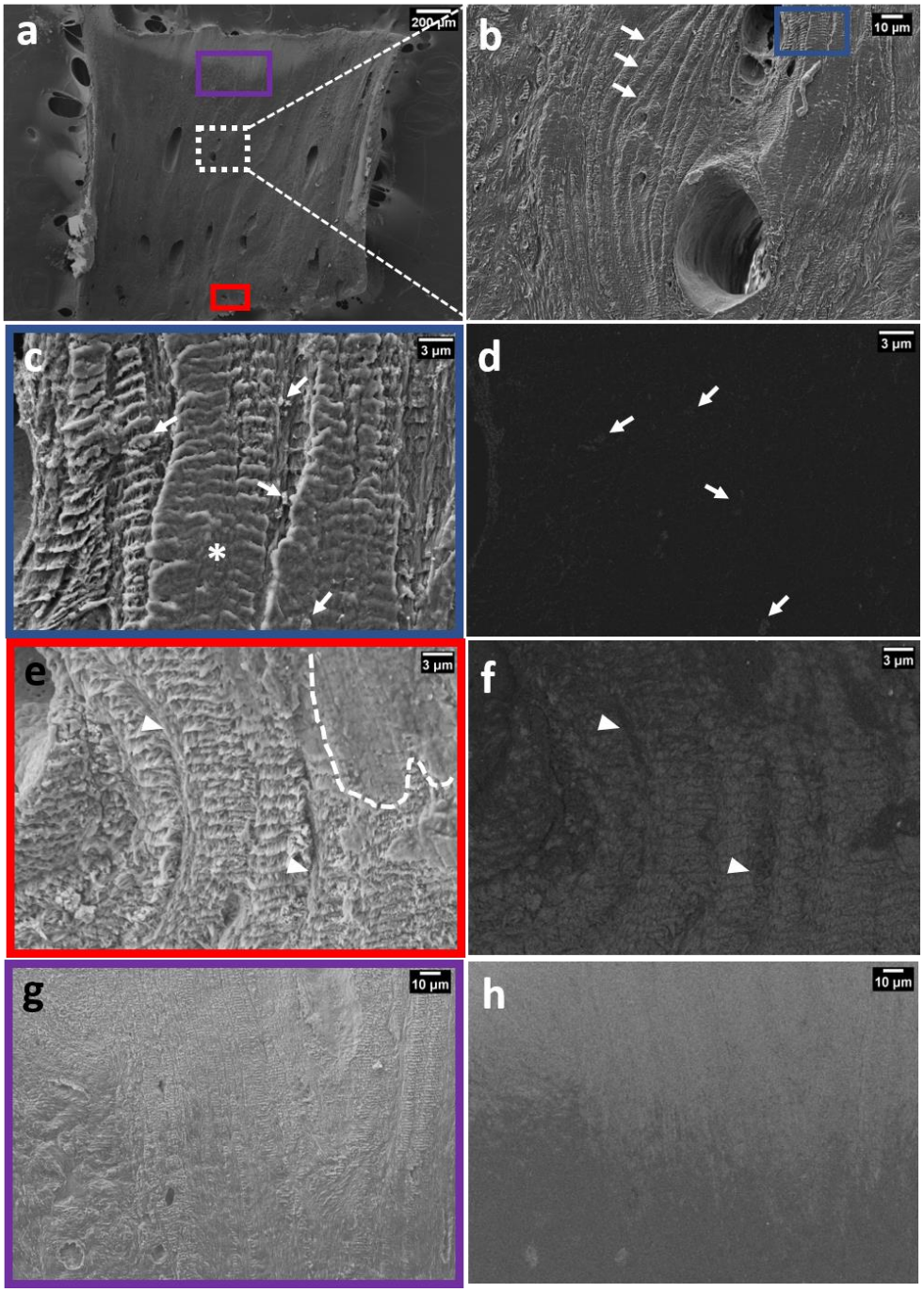

Figure 38. (a) SEM image showing an overview of 1-day remineralized sample. (b) an osteon located in the middle area with successive lamella located concentrically around the haversian canal. (c-d) higher magnification of the area inside the blue box in SE and BSE mode, displaying lamella with collagen fibrils parallel and normal to the imaging plane; white arrows point to small mineral precipitates on the surface; asterisk denotes the loss of collagen microstructure. (e-f) higher magnification of the area inside the purple box in SE and BSE mode; white arrow heads point to lamella with collagen fibrils parallel to the surface which show lower degree of mineralization. (g-h) higher magnification of the area inside the red box in SE and BSE mode displaying continuous mineralization from the sample edge towards the center.

6-day mineralization

The results of mineralization after 6 days are presented in fig 39. Similar to what was done in the 1-day experiment, the area around an osteon was investigated (fig 39a). A closer look at the marked stand-alone collagen fibre in fig. 39b displays striking similarities with what is observed in natural human bone (fig 39c). Comparing the collagen fibre with the control in fig 39c, we see the same rough texture of the bundled fibrils along with many needle like as well as clusters of crystallites precipitated on the surface. *Rodriguez et al.*[37] observed similar rough texture while mineralizing collagen sponges with osteopontin as the directing agent. They claimed the bulges observed in the collagen fibrils to be due to uneven infiltration of the minerals into the fibrils which become visible after drying and exposure to vacuum in SEM chamber. The regions infiltrated with minerals retain their structure while the nonmineralized or less-mineralized regions collapse upon drying. Despite being an artefact, Rodriguez and co-workers claimed this to be evidence of mineral infiltration into the fibril. However, unlike this research, they were not able to observe a similar effect while remineralizing bovine femur bone slices due to the dense nature of natural collagen substrate.

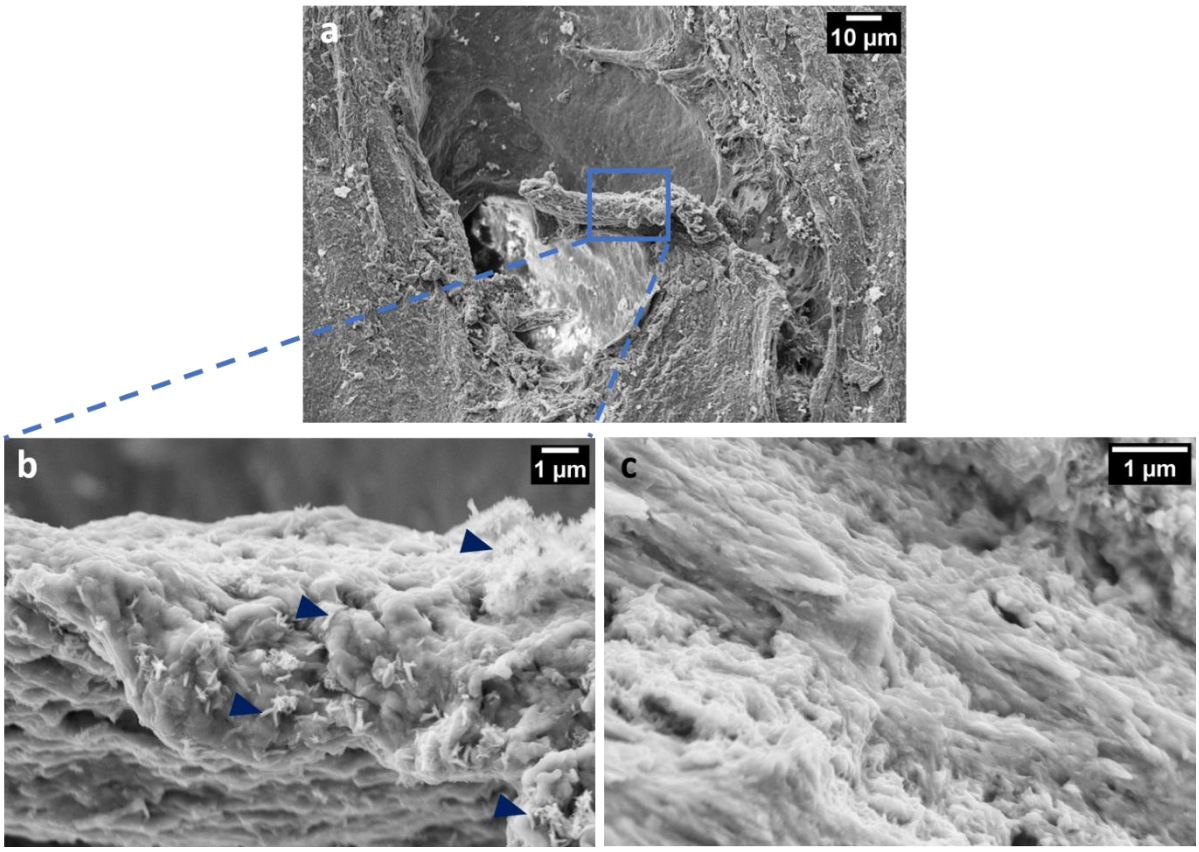

Figure 39. (a) SEM image showing an overview of 6-day remineralized sample. (b) higher magnification of the area inside the blue box displaying a stand-alone mineralized fibre displaying similar texture to natural human bone depicted in (c). Dark blue arrow-heads point to random needle-like as well as clusters of mineral precipitates.

Moving to areas with less radical structures, we see clear evidence of the mineralization progress compared to what we saw after 1 day. Fig 40(a-b) shows such an area. Higher magnification displayed in fig 40(c-d) reveals that while the precipitations in the non-mineralized areas are very much random, the mineralized areas contain extrafibrillar minerals aligned with the collagen fibrils and filling the gap in between them. It is also noteworthy that in some regions such as in fig 40 (e-f), we seem to lose the outline of the collagen since a thin layer of mineral coating covers the fibril.

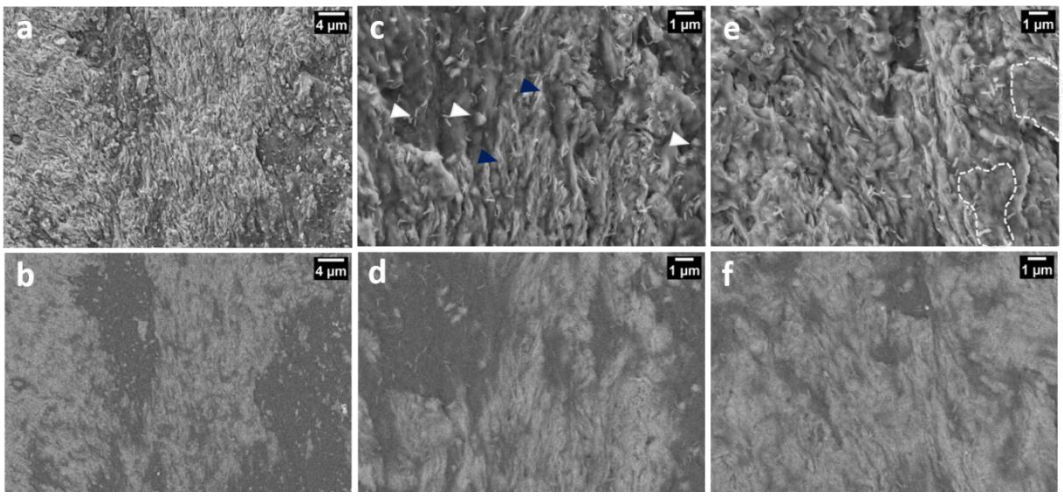

Figure 40. (a-b) SEM image showing a remineralized region on day 6 in SE and BSE mode. (c-d) higher magnification of an area in SE and BSE mode displaying random spherical and needle-like crystal precipitates in non-mineralized regions (white arrow-heads) and oriented mineral platelets located in extrafibrillar gaps between the collagen fibrils (dark blue arrow-heads), (f-g) a mineralized area where some collagen fibrils display loss of texture due to a thin layer of mineral coating (area inside the dashed lines).

Determination of required mineralization period

The results presented for 1-day and 6-day mineralization suggested that the experiments are successful. The next step was to determine how long the remineralization process needs to take place in order to reach a mineral content similar to natural bone. To do this, we repeated the experiment for 1 day and 3 days and preformed ATR-FTIR spectroscopy on the mineralized samples as well as the control. The mineral/matrix ratio (M/M) that expresses the proportion of the mineral content to organic content of the bone could be readily calculated by integrating the areas under the $\nu_1, \nu_3\ PO_4^{3-}$ peak and amide I peak.[67] Therefore, it proves to be a convenient and effective way to express how far the mineralization has proceeded. Moreover, contrary to the 1-day and 6-day remineralized samples which were only very briefly soaked in deionized water, the samples used for FTIR spectroscopy were thoroughly washed in order to rinse away the mineralization solution together with the crystal precipitations as much as possible and thereby avoid any false signal associated with presence of the crystallites on the surface.

Fig 41 shows the FTIR spectra of the control (a) together with the samples mineralized for 1 day (b) and 3 days (c) respectively. In all three spectra, a similar baseline subtraction has been performed. The areas under the peaks located at 1647, 1633, 1637 cm^{-1} (amide I peaks) and peaks located at 1016, 1018, 1019 cm^{-1} (highest phosphate peaks) were used to determine the M/M ratios.

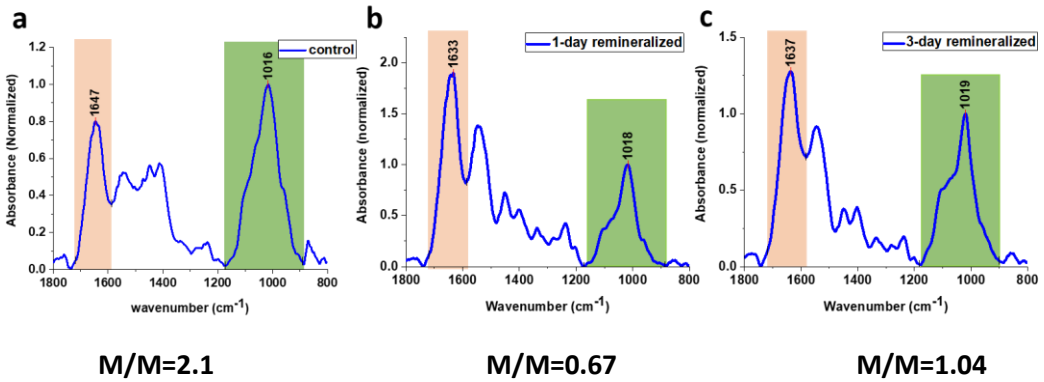

Figure 41. FTIR spectra of (a) control, (b) 1-day remineralized and (c) 3-day remineralized samples.

The mineral to matrix ratio of the control sample was 2.1, while the ratio for the 1-day and 3-day remineralized samples were 0.67 and 1.04, respectively. Based on this progression trend, we decided upon a period between 7-9 days to be a sufficient amount of time to reach the M/M ratio of natural bone.

8-day mineralization

Fig 42 shows the IR spectrum of the sample after remineralization for 8 days. The M/M ratio for this spectrum turned out to be about 0.53 which was even less than the ratio obtained after 1 day of remineralization.

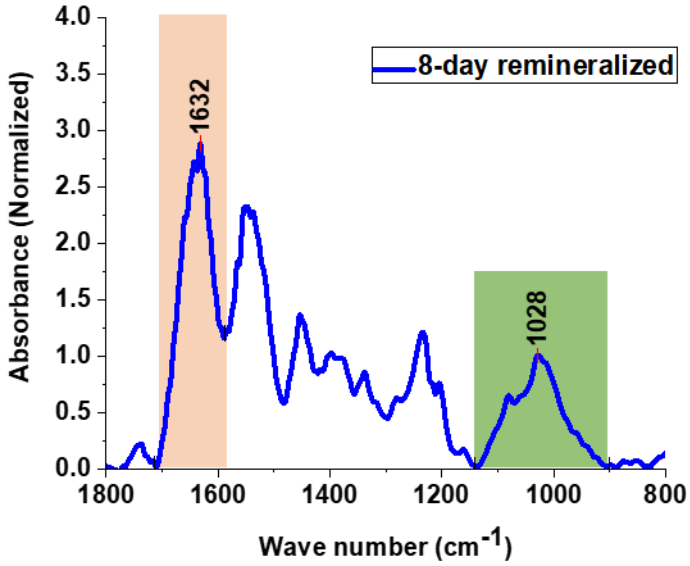

M/M=0.53

Figure 42. FTIR spectrum of 8-day remineralized sample

This outcome initially seemed unreasonable. Therefore, we moved to further investigate the sample via SEM. Comparing spatial distribution of the minerals in the 3-, 6- and 8-day remineralized samples presented in fig 43 provides a possible explanation for this unexpected result for M/M ratio: The nonhomogeneous nature of the mineral distribution on the sample surface is evident in all 3 samples. Mineralization seems to have started at several locations on day 3 with little progression due to short mineralization period. On day 6, the mineral patches have covered a significantly larger surface area and the texture of the collagen fibrils are still visible. On day 8, it appears that instead of increasing the surface coverage, the mineralization has predominantly progressed in the form of densification of these randomly distributed patches.

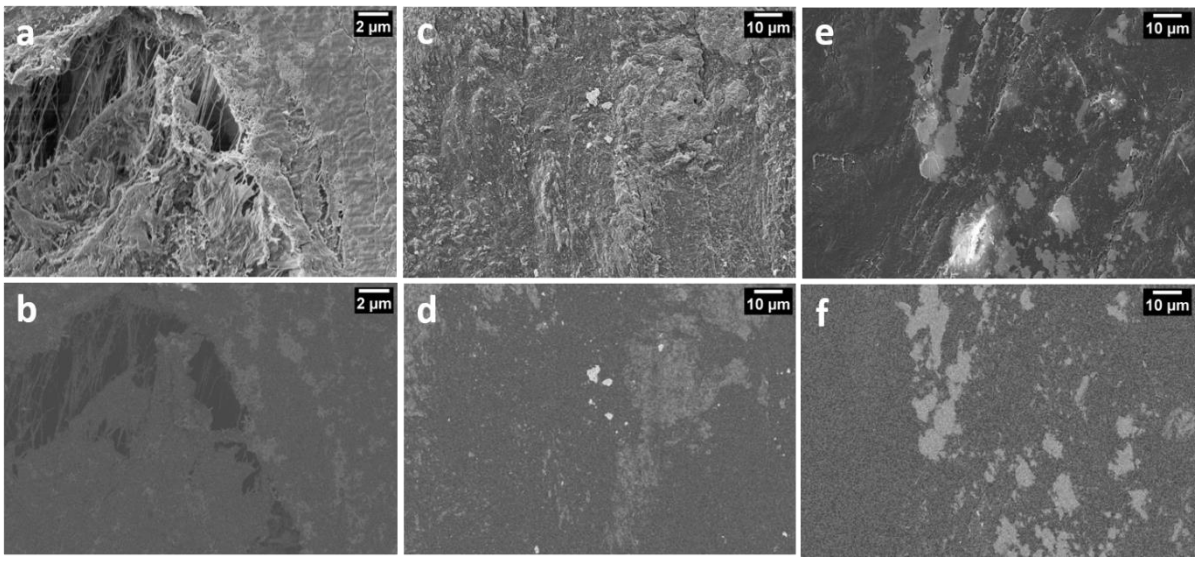

Figure 43. SEM micrographs showing heterogeneous distribution of mineral patches after 3 days (a-b), 6 days (c-d) and 8 days (e-f) of remineralization

The operating principle of ATR-FTIR is based on successive attenuation of the internally reflected light when it hits the interface between the sample and the crystal.[52] This fact together with the heterogeneous distribution of mineral patches on sample surface could be why the results for M/M ratio were not as anticipated. Usually, the most reliable M/M ratios from ATR-FTIR spectroscopy are obtained from powdered samples. By crushing the sample into a powder, the material will be homogenized and therefore a more accurate measurement could be performed.[52] However, since further investigation of the tissue was necessary here, this was no option. Furthermore, rotating the sample on the crystal resulted in varying signal intensities with some cases without any peak between 900-1200 cm^{-1} proving that the point of contact between the sample surface and the crystal has a significant impact on the outcome. As a conclusion, we suggest that for this strategy to be reliable, the samples that are being used to determine the end-point of mineralization should all be made into powder. Only after determining the accurate mineralization period based on the powdered samples, will it be plausible to keep the sample intact for later SEM investigation.

Thresholding the BSE images

Even though the end-point determined for the experiment did not reflect a mineral content comparable to that of natural bone, we still proceeded with comparing the mineralized areas with our control. It was already mentioned that BSE imaging is an effective way for determining where the minerals are located. However, the brightness and contrast settings used during imaging, the selected noise reduction method, duration of imaging and pixel dwelling time, all have a significant impact on the range and distribution of the gray values throughout the image. As a result, for any set of settings, the range of gray values that represents the minerals would be different. Hence, we decided to use the exact same settings for imaging the control and the 8-day mineralized sample so as to be able to define a certain range of gray values that we claimed represent the minerals.

The samples under investigation contain holes, non-mineralized collagen, and mineralized collagen. While the holes represent the lower limit of the gray values, we felt the need to have an upper limit that would help us adjust the brightness and contrast effectively, without saturating the signal

corresponding to the minerals. To this end, we stained the edges of the samples with silver paste. Being an element with high atomic number, silver gives off a significantly more intense signal in BSE images. Hence, we used it to set the upper limit for our BSE imaging.

Fig 44 displays the steps we have taken to assign a certain range of gray values to each element present in the samples. In fig 44a, we see homogeneous signal intensity throughout the image with the exception of an intense signal representing the silver paste. The histogram is given in fig 44b where we see two distinct peaks at 117 and 234 positioned far away from each other. The first peak was assigned to non-mineralized collagen while the second peak was assigned to silver. To define a certain thresholding value for the mineralized collagen, an area with high surface coverage of minerals was selected (fig 44c). The histogram for this area displays two distinct peaks close to each other (fig 44d). The first one is roughly positioned at the same gray value as fig 44b. The second one at 150 is thus assigned to the mineralized area. A third area containing all 3 different regions was also chosen (fig 44e) to validate the assigned peaks. The histogram for this region displays the two distinct peaks assigned to non-mineralized collagen and silver, as well as a shoulder for the mineralized areas centralized around 150.

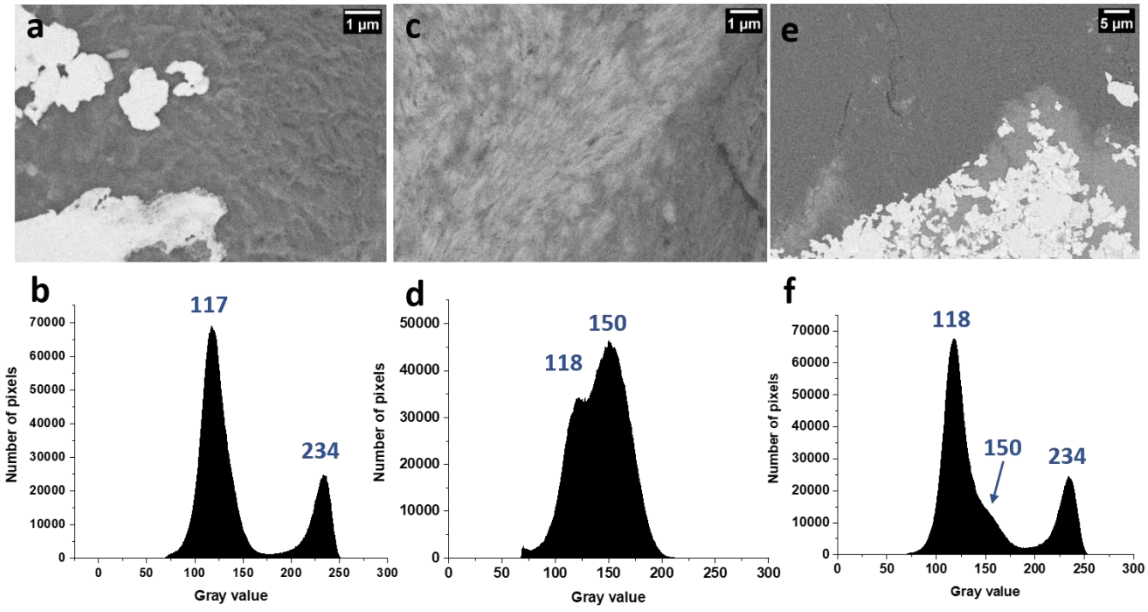

Figure 44. (a,c,e) BSE images of several regions containing various compositions of silver, mineralized and non-mineralized collagen. (b,d,f) histograms corresponding to (a,c,e) respectively.

Concluding this section, fig 45 shows the threshold specification which will be used in further analysis of the mineralized areas. Gray values in the range 0-118 are assigned to holes. Gray values in 119-150 range represent non-mineralized collagen. The mineralized areas have gray values in the range 151-202 and finally signals corresponding to silver could be represented in the gray value range above 202.

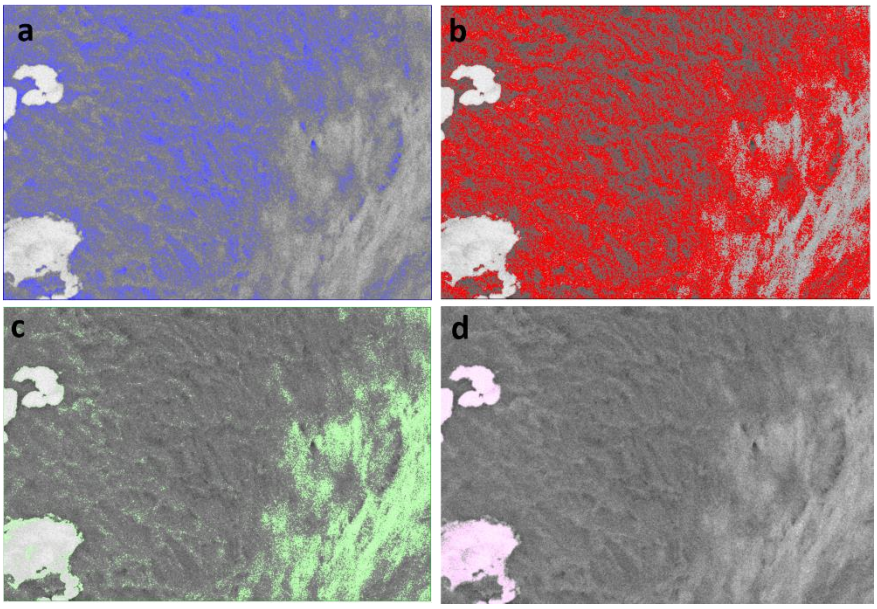

Figure 45. A representative BSE image with thresholds applied to define empty regions (a), non-mineralized collagen (b), mineralized collagen (c), silver paste (d)

8-day remineralized vs. control

Fig 46b shows the overlay of BSE image onto the SE image represented in fig 46a. The interface between the mineralized and non-mineralized area is evident. Contrary to what we observed in 1-day remineralized sample (fig 38e, 38f), here we can see that the fibrils parallel to the surface are more mineralized compared to the ones normal to it. In addition, the fibrils sticking out show non-mineralized tips while we see mineral deposition further down their length. This observation could be explained based on the infiltration mechanism described by *Nudelman et al.*[27], stating that the minerals infiltrate the fibrils in the gap zones from the fibril side and not its edge. However, The discrepancy observed between 1-day and 8-day mineralized samples leads us to believe that the degree of surface exposure to the mineralization solution previously mentioned, may not be the sole limiting factor and other more decisive factors may be in play. It could be that the maturity of the collagen fibrils and the extent of their crosslinks are spatially different throughout the sample and the areas that are more strongly crosslinked, inhibit the infiltration of the mineral components.

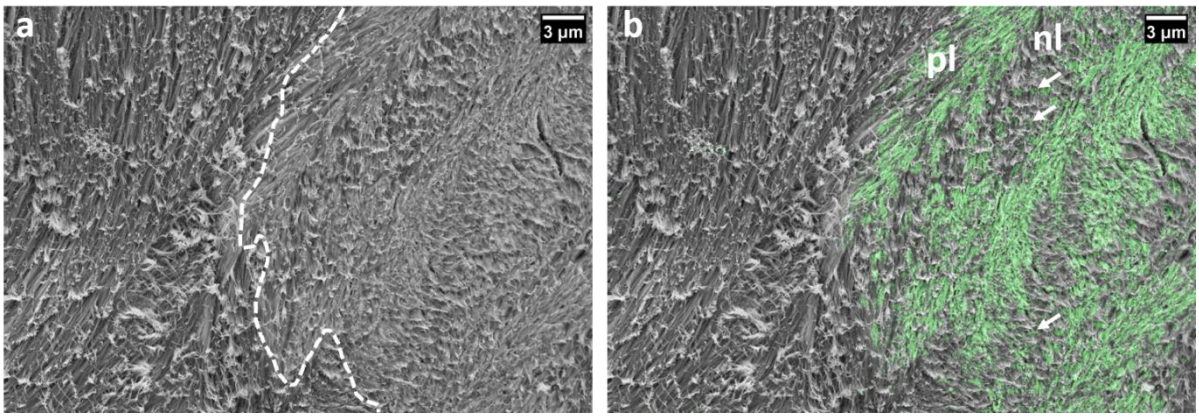

Figure 46. (a) SEM image of the sample after 8 days of mineralization; the white dashed line denotes the mineralization front. (b) BSE image of (a) overlaid on top (the green signal) displaying the mineral distribution in collagen fibrils parallel (pl) and normal (nl) to the imaging plane. White arrows point to minerals located along the collagen fibrils normal to the imaging plane.

A closer look at the interface and the overlay with corresponding BSE image are given in fig 47 (a-b). The banding pattern of the non-mineralized collagen is clearly visible in fig 47a with a mineralized one immediately next to it. The mineralized fibrils look well extended with a smooth surface which could be an indication of even infiltration of mineral into the fibril.[37] The fact that we do not see any mineral clusters deposited on the surface, further reinforces the intrafibrillar mineralization assumption.[38] The comparison between biomineralized (fig 47(c-d)), non-mineralized and remineralized fibril given in fig 47 shows that naturally mineralized fibrils look thicker probably due to higher degree of mineralization. In fact, comparing the size of the distinguishable fibrils in remineralized sample and control suggests that what we see in control is actually bundles of collagen fibrils which have been cemented together by an external layer of mineral deposition and thus hiding their outline.

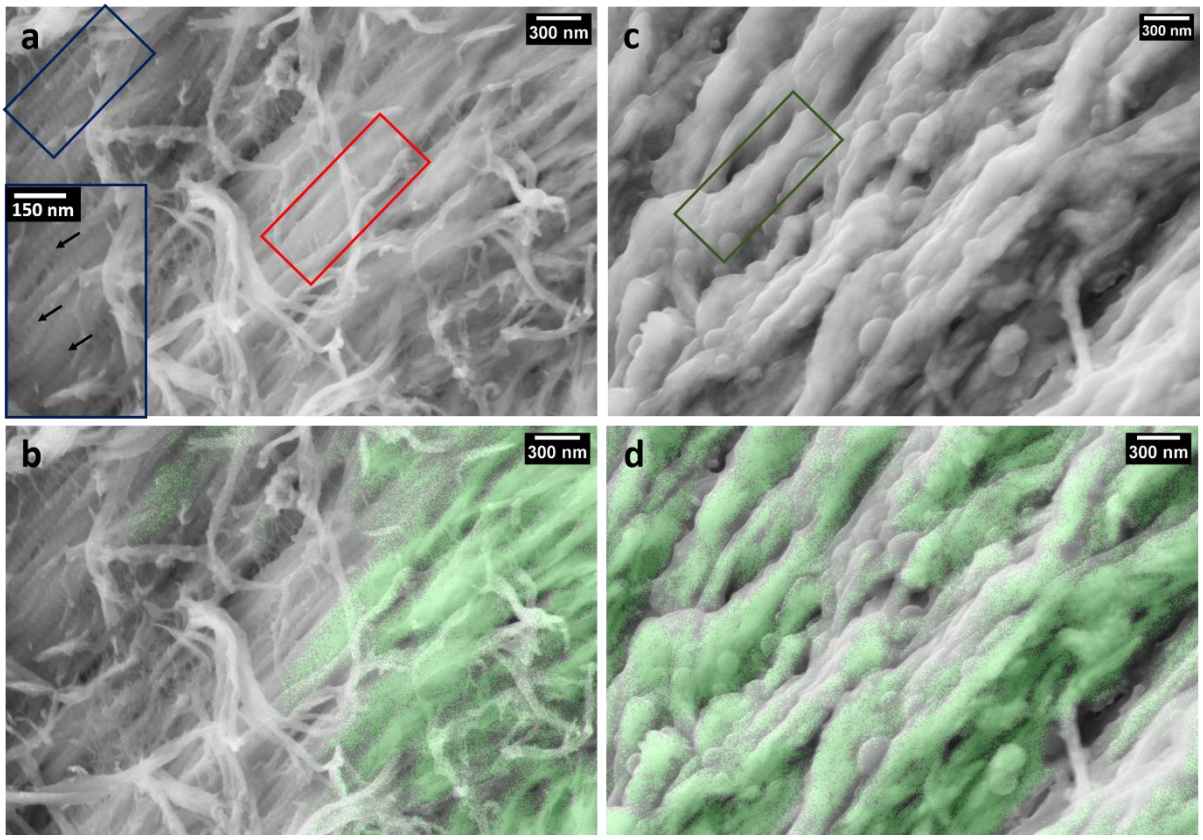

Figure 47. SEM micrographs comparing non-mineralized and remineralized collagen fibrils (a,b) with bio-mineralized fibrils (c,d). the blue, red and green boxes outline the non-mineralized, remineralized and biomineralized fibrils respectively. The black arrow points to the collagen fibril banding pattern.

Even though further investigation of dense mineral patches with SEM does not reveal any further in detail information on the morphology, it could very well be that the collagen fibrils lying beneath these dense mineral patches are similar to what we see in the control. In other words, what we see in our control, seems to lie somewhere in between what was observed in day 6 and day 8.

Conclusively, we suggest that the mineralization of collagen fibrils may temporally evolve in the order shown in fig 48. Initially, intrafibrillar mineralization occurs with no significant change in the texture and architecture of the fibrils. The only visible difference is the fading of the collagen banding pattern as well as enhance signal in BSE image indicating the presence of the mineral. As mineralization continues, need-like minerals stack and fuse together forming mineral platelets filling the spaces in between fibrils and as was suggested by *Reznikov et al.*[23], will weave around the fibrils forming a continuous layer and thickening the fibrils as it is seen in the control. Finally, prolonging the

mineralization leads to further deposition of minerals on the fibrils forming dense patches completely hiding the mineralized fibrils underneath.

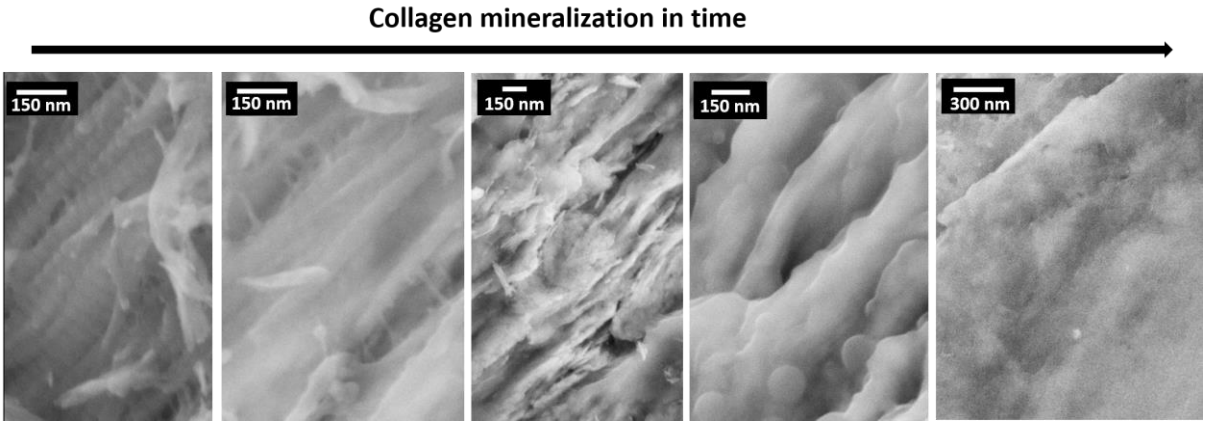

Figure 48. Temporal evolution of in-vitro mineralization in tissue-based collagen

Formation and maturation of minerals

The previously obtained FTIR spectra could be used to study the differences that exist between the natural and in-vitro created minerals. Fig 49 displays the spectrum for each case normalized to the amide I peak. The peaks that represent the CO_3^{2-} vibrational modes are lower in intensity in the remineralized samples. This is expected because the mineralization solution did not contain any component that would serve as a source for carbonate and be responsible for its subsequent substitution into the hydroxyapatite lattice. The peaks around 1410 cm^{-1} and 1450 cm^{-1} are still visible but due to their low intensity, it is reasonable to assume that they are representing the CH_2 wagging and bending vibrations. In the control, these bands are superimposed with that of the CO_3^{2-} and thus show a higher intensity.[51] The absorbtion at 1566 cm^{-1} denoting the type A carbonated apatite is not observed in the remineralized samples either.

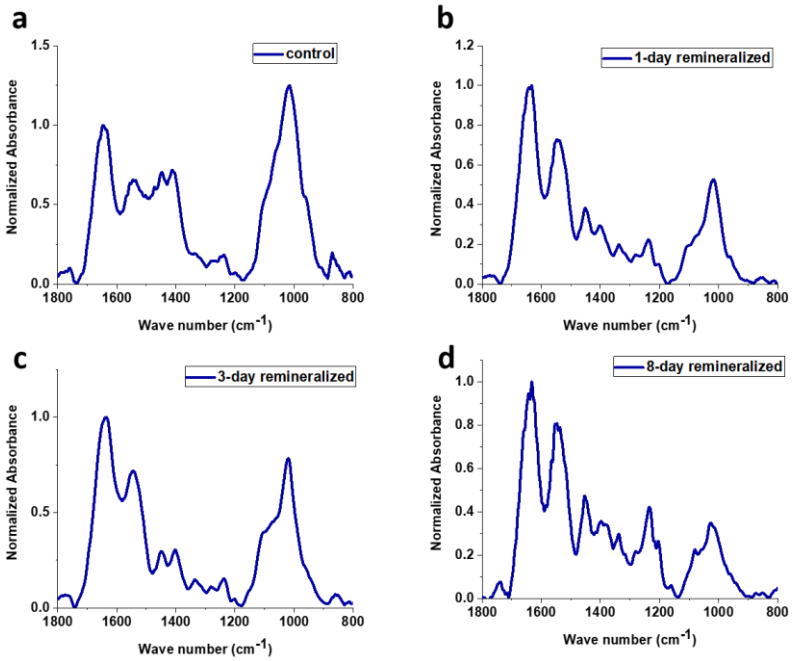

Figure 49. FTIR spectra of (a) control, (b) 1-day remineralized, (c) 3-day remineralized and (d) 8-day remineralized samples. All spectra are normalized to the amide I peak position at 1640 cm^{-1}.

A closer look at the 900-1200 cm^{-1} region and the $\nu_2\ CO_3^{2-}$ band at 870 cm^{-1} are illustrated in fig 50. The reduced absorption at 870 cm^{-1} in the remineralized samples supports the previous claim that fewer carbonate ions are present in the structure of the created minerals. As a result, we can reasonably conclude that the majority of the imperfections that are present in the crystal lattic of the created HA, are most probably caused by acid phosphate substitution.

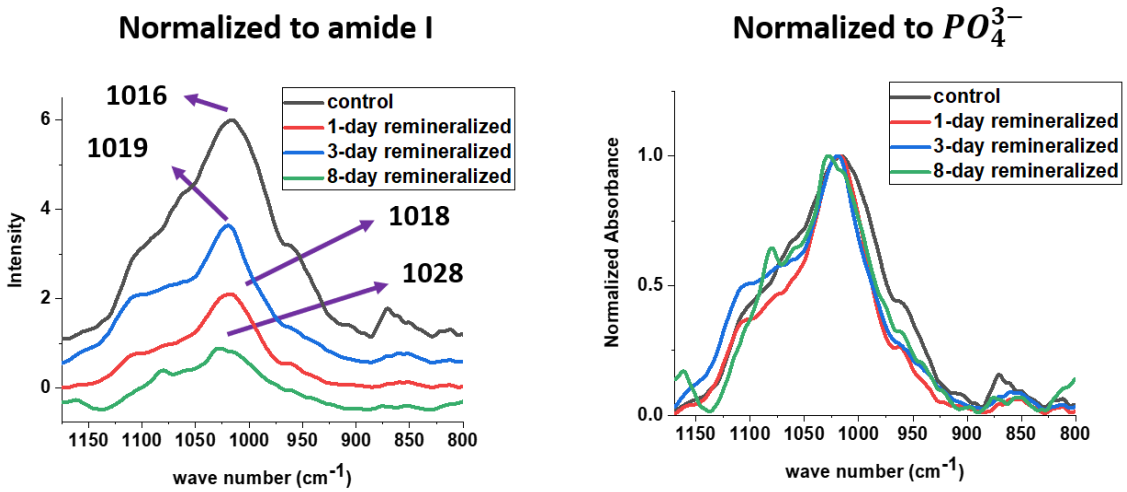

Figure 50. FTIR spectra illustrating the shape of the peaks denoting phosphate and carbonate vibrations in the 800-1170 cm^{-1} region.

It appears that as mineralization proceeds, the peak in 900-1200 cm^{-1} region is shifting towards higher wave numbers with the 8-day remineralized sample possessing a peak very close to 1030 cm^{-1} which has been assigned to apatitic phosphate groups and is representative for highly crystalline stoichiometric HA.[71] A concomittant occurrence along this peak shift is the gradual disappearance of the shoulder around 1110 cm^{-1}. This peak denotes the presence of poorly crystalline apatites and emerges due to the substitution of acidic phosphates in the HA crystal lattice.[71] For the samples mineralized for 1 day and 3 days, this shoulder in the spectrum is visible even without deconvolution. For the control, it seems to be overlapped by other underlying sub-bands. However, it is barely visible in the case of 8-day mineralization, resulting in an overall narrower band compared to the others.

Conclusion

In this chapter, we have first investigated the demineralization of human cortical bone using EDTA with the goal of achieving close to complete demineralization of the bone tissue while keeping the morphology and structure of the organic matrix intact. Using ICP-OES we were able to analyze the dynamics of the demineralization process. This showed that using 9.5% EDTA at 4°C, demineralization of 99.1% could be achieved after 12 days. This result was validated with ATR-FTIR, in which no phosphate related peaks were detected in IR spectrum. Additionally, the spectrum was very similar to a reference spectrum for collagen type I, suggesting no significant chemical changes in the organic phase as a result of the demineralization process. The ultrastructure of the organic matrix was investigated using SEM. All the characteristic features of bone were still observed and no significant changes were noticed as compared to what has been reported in literature. Furthermore, the backscattered electron images also verified the absence of high atomic number elements (Calcium) in the studied areas.

In-vitro mineralization was first attempted on 210 nm thin sections of dense biogenic collagen so as not to complicate the process with diffusion limitations. The ultrathin samples were successfully remineralized on a TEM grid. BF-TEM imaging confirmed the demineralized nature of the sections prior to the experiment, as well as their remineralization after the experiment. The nature of this mineral phase was determined to be hydroxyapatite by SAED pattern analysis. Furthermore, the positioning of the (002) plane reflection in the SAED pattern revealed the preferred orientation of the HA c-axis which was in line with the dominant direction of collagen fibrils. Comparison between the SAED pattern of the remineralized sections and that of natural human bone revealed remarkable similarities further reinforcing the successful remineralization. However, despite the gathered evidence on the phase and orientation of the created minerals, it is important to note that regular 2D TEM imaging is not sufficient to determine whether the mineralization has occurred inside the collagen fibrils or not. 3D reconstructions and electron tomography is required for this purpose.

Following the successful remineralization of the dense biogenic collagen substrate on a TEM grid, same experiment was conducted on sections with 100 μm thickness. After 1 day and 6 days, SEM imaging in SE mode revealed the ultrastructure of mineralized regions on the sample while imaging in BSE mode confirmed the presence of mineral phase as well as its spatial distribution. 1-day remineralization mostly displayed mineralization around the edges of the sample while 6-day remineralization exhibited significant similarities with natural bone in terms of the texture of the mineralized collagen fibers. Furthermore, the rough texture of the collagen fibrils presented a probable indication for successful intrafibrillar mineralization. Next, ATR-FTIR spectroscopy was used to study the degree of mineralization at different time points and determine the reasonable mineralization period that would allow us to achieve a mineral content comparable to that of naturally mineralized bone tissue. The samples were mineralized for 1 day and 3 days and their M/M ratio was compared to a control. On this basis, a period of 8 days was deemed a reasonable time for mineralization.

Comparisons between the ultrastructure and spatial distribution of mineralized regions after 8 days of remineralization and the control was done by unifying the imaging parameters in terms of brightness, contrast, noise reduction method and imaging times. On this basis, a certain range of gray values was designated to each phase allowing us to pinpoint the mineralization fronts and the differences in the degree of mineralization in natural bone and remineralized bone. Additionally, this comparison allowed us to propose a model for temporal evolution of collagen structure over the course of mineralization.

Finally, the FTIR spectra for different time points were then analyzed based on presence/absence of certain bands that are assigned to several significant vibrational modes that allow us to get information about the nature and composition of the crystals and their maturity. The diminished intensity of carbonate vibrational bands indicated that negligible structural defects were present in the in-vitro created HA crystals due to carbonate substitution, leaving mostly the acid phosphates as the source for nonapatitic/poorly crystalline crystals. This was confirmed by the presence of a band around 1100-1110 cm^{-1} denoting the HPO_4^{2-} vibration mode which disappears in the 8 day mineralized sample. This fact together with the resemblance between the $\nu_1, \nu_3\ PO_4^{3-}$ band shape with that of a sintered synthesized apatite indicates the presence of highly stoichiometric HA crystals after 8 days of mineralization.

Chapter 4. Conclusion and outlook

The aim of this project was to emulate the natural process of bone mineralization using a tissue-based collagen substrate derived from human cortical bone. Microscopic techniques were used for studying the ultrastructure and morphological evolution of the samples. FTIR analysis was used to study the properties and nature of the mineral phase.

Due to the intimate relation between collagen and minerals, we first applied a simple deproteinization technique in order to isolate the mineral phase. By doing so, we were able to clearly visualize the ultrastructure of the minerals via SEM and investigate the morphological evolution of the mineral from bone apposition to maturation. We observed that even in the absence of the organic phase, the mineral phase perfectly maintains its structural integrity and at each location, mostly follows the dominant direction of collagen fibrils in that location.

In order to perform in-vitro mineralization, we required the biogenic collagen substrate completely devoid of natural minerals. Therefore, we studied the dynamics of demineralization using ICP-OES to ensure thorough demineralization of the samples. Further SEM and FTIR measurements validated the completion.

Prior to bulk remineralization of the dense collagen substrate, we aimed to ensure that mineralization on the nanoscale is comparable to natural bone, in terms of type of mineral formed and orientation of the mineral crystals within the collagen structure. To this end, we prepared 210 nm thin sections of the demineralized specimens and remineralized them on a TEM grid. BF-TEM images revealed high amount of mineralization after 2 hours. Additionally, SAED pattern analysis revealed the phase of the created minerals as HA with their c-axis parallel to the collagen fibrils.

Bulk remineralization of the tissue-based collagen substrate was performed for different time points. After each experiment, we used SEM in SE and BSE mode to investigate the ultrastructure and mineral distribution, respectively. Through SEM micrographs in SE mode, we were able to establish a likely temporal evolution of mineralization in collagen fibrils and based on BSE images, we clearly observed the spatial distribution of minerals at each location. Furthermore, by applying a unit thresholding criterion, we were able to reliably compare and analyze the BSE images of different samples while determining mineral distribution and pinpointing mineralization fronts in each one of them.

The fact that complete infiltration of mineral components into the collagen substrate is not an issue in-vivo, further backs up the results of this work and proves its success in mimicking the natural mineralization process. In fact, Akiva et al.[72] showed that the continuously produced mineral components are transported and delivered to mineralization fronts via intercellular pathways that connect the arteries to bone matrix. Hence, as far as penetration depth is concerned in in-vitro mineralization, achieving a penetration depth comparable to lamellar thickness would be deemed sufficient.

In conclusion, we have shown that bone-like micro- and nanostructure can be replicated in biogenic collagen substrates by using a supersaturated mineralization solution that contains calcium and phosphate ions as well as poly aspartic acid as the mineral directing agent. This method can be used to artificially mineralize any kind of collagen-based substrate for applications such as production of bone and dental implants.

This successful in-vitro reconstitution of bone biomineralization allows us to now investigate other aspects of the process that remain unresolved. For instance, the degree of the supersaturation in mineralization solution could be of relevance for the abundance of different apatite compounds that

are created in-vitro. Therefore, different mineralization solutions containing various ratios of calcium and phosphate ions could be used and the mineralization results could be correlated with the supersaturation index of the solution relative to hydroxyapatite to ensure that bone-like apatite is being created. However, as it was explained in this work, ATR-FTIR may not be a reliable method to study the mineral content of the remineralized specimens. Other more destructive techniques such as thermogravimetric analysis (TGA) could be applied to determine the mineral content more accurately. Furthermore, the penetration depth of the mineralization solution into the dense collagen scaffold could be monitored to see if there exists a correlation between this depth and lamellar thickness or the crosslinking of the collagen fibrils.

The usefulness of scanning electron microscopy in studying bone mineralization is already indisputable. However, incorporating different modes into regular SEM could significantly improve the results. As it was briefly described, cryo-SEM could be used to keep the biogenic tissue in its native state and perform the remineralization process step by step in order to follow it through time. Furthermore, cryo-SEM does not require fixation of biological specimens which would be an advantage for better emulating the natural mineralization process. The possibility for freeze fracturing inside the chamber also eliminates the loss of microstructure as was observed using the vibratome in this work. Finally, combining cryo-SEM with quantitative backscattered electron imaging (qBEI) would help shed light into the density distribution of bone minerals following remineralization.

Chapter 5. Experimental

1. Materials

All the chemicals were purchased from Sigma-Aldrich and milliQ-filtered water was used for dilution of stock solutions and the washing steps.

Whole human femurs from a healthy male donor were kindly donated by HCM medical (Nijmegen) which were freshly frozen -20°C. The femur shafts were cut into cubes of approximately 2×2×1 mm dimensions using a hand saw and subsequently were trimmed to the exact mentioned dimensions. The cubes were then fixed with a fixation solution composed of 0.8% paraformaldehyde (PFA) and 0.2% Glutaraldehyde (GA) in PBS buffer at PH 7.4 for 24 hours in room temperature.

Preparation of bone slices

100 μm thick slices of bone were prepared using a Leica VT1000S vibratome. Following fixation, the bone cubes were attached to a metal plate using acrylate glue. Once the glue was dried, the plate was mounted into the vibratome sample holder and the set-up was submerged in PBS. Slicing was done with the speed and vibration frequency set to 3.5 and 3, respectively. A steel blade was used for the cutting.

Deproteinization

Following fixation, bone slices were put in a well plate in the cold chamber and 5% sodium hypochlorite (NaOCl) was added to an extent up to which the bone slices were completely submerged. After 48h, the solution was carefully removed and refreshed by slow drop-wise addition. After 72h, NaOCl solution was removed and the slices were carefully washed by very slow addition of milliQ water 5 times. Each time, the sample was soaked for 5 minutes.

Demineralization of bone blocks

Demineralization of bone blocks were carried out in a solution composed of either 9.5% or 5% EDTA, 0.2% PFA and 0.05% GA in PBS buffer at PH 7.4. Two different temperatures (4°C and 25°C) and two different durations (7 days and 12 days) were applied. Each block was submerged in 5ml of demineralization solution. The solution was changed daily except for the weekends.

Demineralization of the bone slices

Bone slices were demineralized in a demineralization solution composed of 9.5% EDTA, 0.2% PFA and 0.05% GA in PBS buffer at PH 7.4 and 4°C for 5 days on a tube roller. Each slice was submerged in 1.5 ml of demineralization solution with daily solution changes. The slices were copiously washed with deionized water following demineralization.

Preparation of ultra-thin slices for TEM

Following demineralization, the bone blocks were infiltrated with sucrose solution for cryoprotection overnight. subsequently, they were positioned on a mounting pin and plunged into liquid Nitrogen. The frozen specimens were then sectioned into 210-nm thin sections with a cryomicrotome. Finally, the samples were transferred to gold TEM grids with holey carbon R2/2.

Dehydration

The samples were dehydrated using graded ethanol (EtOH) series with ascending concentrations of 50%, 75%, 99% and ultra-pure EtOH at 4°C. Each step was performed for 15 minutes. The step with 99% EtOH was performed twice. Due to the very delicate nature of deproteinized samples, no shaking was involved during dehydration. The slices were put in a well plate and the appropriate EtOH solution was carefully deposited on top of the slice one drop at a time. For the rest of the samples, dehydration was done by submerging the samples in the appropriate EtOH solution on a rocking table.

Drying

The deproteinized samples were air dried in the oven at 37°C overnight. The rest of the samples were dried with a SPI-DRY critical point dryer. After dehydration, the samples were quickly transferred to the grid holder and submerged in the cover slip holder that was previously filled with pure EtOH. The cover slip holder was then transferred into the pressure vessel and the vessel was sealed. By simultaneous opening of the inlet and drain valves of CO_2, EtOH was gradually replaced by liquid CO_2 and flushed out of the system. Running CO_2 through the vessel was performed for 4 rounds with a 5-minute pause between two successive rounds.

Remineralization of bone slices

Demineralized samples were remineralized via the PILP process with polyAsp as the process directing agent. The mineralization solution was prepared according to the protocol from Deshpande et al. [19] with the slight change of using K_2HPO_4 instead of $(NH_4)_2HPO_4$ as phosphate source. The solution was prepared by mixing equal amounts of 6.8 mM $CaCl_2$, 4 mM K_2HPO_4, 3.4×PBS buffer (containing 465.43 mM NaCl, 9.12 mM KCl, 6.49 mM KH_2PO_4 and 29.33 mM $Na_2HPO_4.H_2O$) and 400 $\mu g/ml$ polyAsp. Thus, the final solution consisted of 1.67 mM $CaCl_2$, 1 mM K_2HPO_4, 2.28 mM KCl, 116.36 NaCl, 1.62 mM KH_2PO_4, 7.33 mM $Na_2HPO_4.H_2O$ and 100 $\mu g/ml$ polyAsp. The solution was brought up to 37°C before initiating remineralization.

Each slice was then submerged in 1.5 ml of mineralizing solution and was incubated in 37°C to emulate physiological conditions for different time periods. On each day, the Eppendorfs containing the samples were manually shaken. For the 8-day remineralization, the solution was changed on day 4.

Remineralization on TEM grid

2 droplets of the mineralization solution was put on top of the grid holding the sample and the sample was incubated at 37°C for 2 hours. Subsequently, the remaining mineralization solution was blotted and the grids were washed with milliQ water twice and dried.

Solution preparation for ICP measurement

Prior to each solution change over the course of demineralization, 1 ml of the solution was stored at -18°C in the freezer. For ICP measurements, all the samples were first defrosted at room temperature. Subsequently, each solution was acidified with 100 μl of 65% Nitric acid and then diluted to 10 ml. Adding nitric acid to the solution led to crystallization and precipitation of EDTA. Hence, the solutions were centrifuged for 5 minutes and filtered prior to conducting the ICP measurements. A reference sample of the demineralization solution was also measured in case it contained any trace amounts of calcium before any were extracted from the bone specimens. This trace amount was determined to be 0.1589 ppm. For the calculations, this value was deducted from the measured amounts of calcium for the rest of the solutions.

2. Methods

Scanning electron microscopy

Imaging of all the samples was done on a Zeiss Crossbeam 550 equipped with a field-emission gun operating at an acceleration of 5kV, probe current of 67-69 pA and working distance of 10mm. Prior to imaging, a piece of double-sided carbon tape was put on a SEM stub and the dehydrated and dried bone slices were mounted on top of the carbon tape. Subsequently, the samples were sputter-coated with a (Leica ACE600) twice, with each step adding an 8 nm-thick layer of carbon coating on the sample surface leading to a total of 16 nm-thick layer of coating.

Fourier transform infrared spectroscopy

The IR spectra of the bone slices were generated using a Spectrum One ATR-FTIR (Perkin-Elmer) with a diamond/ZnSe ATR crystal. The spectra were measured in the 400-4000 cm^{-1} wave number range. The dehydrated and dried bone slices were positioned on the crystal, taking care that the crystal was thoroughly covered. The force on the pressure arm was adjusted so that a spectrum with reasonable intensity could be obtained.

Inductively coupled plasma spectroscopy

Measuring the amount of resorbed calcium from the bone specimens was done using the ICAP 6000 (Thermo Fisher scientific, Bremen, Germany) ICP-OES spectrometer equipped with a vertical torch and a radial plasma observation. The solution is placed in a test tube which is automatically transferred into the ICP apparatus by an auto sampler.

Transmission electron microscopy

TEM was done on 210 nm-thin demineralized and unstained bone sections with a JEOL JEM-1400 Flash equipped with Matataki Flash sCMOS camera. Imaging was done at 120 kV operating voltage.

Acknowledgement

From what I have heard, this section is not supposed to be too long in a master thesis. However, the completion of my thesis without the help and support of some people would have been absolutely impossible and this thesis would not be complete without expressing my gratitude to them.

I want to thank Dr. Anat Akiva for everything she has taught me during the past year. Her above and beyond support, both academically and emotionally, leaves me without any suitable words to thank her. Anat, you are the embodiment of everything I want to become and all the things I want to achieve in my future. Thank you for everything.

I would also like to thank prof. Nico Sommerdijk, firstly for going through all the trouble to make my research and presence possible in Radboudumc and secondly, for all his support, valuable ideas, critical analysis of my results and all his efforts for making me a better researcher. Nico, you were like a fairy godfather to me, always with a smile on your face, waving your magic wand to provide exceptional academic and career opportunities for me. Words do not suffice to express my gratitude.

Robin, thank you for guiding my thoughts and efforts in the path to complete my research. I truly appreciate all the weekends and late evenings that you spared to help me finish my report (without even a hint of an anger) as well as tolerating my frantic phone calls whenever I feared I would not make it. I was your first student. I hope the next ones will be much less of a trouble!

I would also like to thank the amazing people in our research group who were like a family to me in Nijmegen: Raquel, my complaining buddy, thank you for listening to my endless whining when things didn't go my way. Marit, you were like a big sister to me, thank you for your support and opening your house to me in my time of need. Judith, you are a genius and always have an answer or a solution for everything. Thank you for all your help. And Luco, thank you for all your help with my research and TEM imaging and also for constantly reminding me what a good supervisor Robin is!

Nilgoon, Salar, Mr Talei and Mrs. Molayi, without your tireless efforts, I would not have been able to come to the Netherlands. Thank you for helping me achieve my dreams. I will forever be in your debt.

My dear parents, I am so sorry I was not able to be beside you in your time of sickness in these times of Corona. You are the best parents any daughter could ask for. Your support, even when you were sick, and your encouraging and reassuring words were what kept me going specially during the past couple of months. I cannot even begin to thank you for everything you have sacrificed for me to be here. I love you both to the moon.

Last but not least, I would like to thank prof. Jan van Hest for accepting to be my graduation supervisor in Eindhoven and make this research possible.

References

1. Olszta, M. J. *et al.* Bone structure and formation: A new perspective. *Mater. Sci. Eng. R Reports* **58**, 77–116 (2007).

2. An, Y. H. & Martin, K. L. *Handbook of Histology Methods for Bone and Cartilage*. *Handbook of Histology Methods for Bone and Cartilage* (2003). doi:10.1385/1592594174

3. Lisowska, B., Kosson, D. & Domaracka, K. Lights and shadows of NSAIDs in bone healing: the role of prostaglandins in bone metabolism. *Drug Des. Devel. Ther.* **Volume 12**, 1753–1758 (2018).

4. Bartl, R. & Bartl, C. *Bone Disorders*. *Bone Disorders: Biology, Diagnosis, Prevention, Therapy* (Springer International Publishing, 2017). doi:10.1007/978-3-319-29182-6

5. Long, F. Building strong bones: molecular regulation of the osteoblast lineage. *Nat. Rev. Mol. Cell Biol.* **13**, 27–38 (2012).

6. Reznikov, N., Shahar, R. & Weiner, S. Bone hierarchical structure in three dimensions. *Acta Biomater.* **10**, 3815–3826 (2014).

7. Wang, X. *et al.* Topological design and additive manufacturing of porous metals for bone scaffolds and orthopaedic implants: A review. *Biomaterials* **83**, 127–141 (2016).

8. Beniash, E. Biominerals-hierarchical nanocomposites: The example of bone. *Wiley Interdiscip. Rev. Nanomedicine Nanobiotechnology* **3**, 47–69 (2011).

9. Gao, C., Peng, S., Feng, P. & Shuai, C. Bone biomaterials and interactions with stem cells. *Bone Res.* **5**, 17059 (2017).

10. Vandecandelaere, N., Rey, C. & Drouet, C. Biomimetic apatite-based biomaterials: On the critical impact of synthesis and post-synthesis parameters. *J. Mater. Sci. Mater. Med.* **23**, 2593–2606 (2012).

11. Stock, S. R. The Mineral–Collagen Interface in Bone. *Calcif. Tissue Int.* **97**, 262–280 (2015).

12. Shah, F. A., Zanghellini, E., Matic, A., Thomsen, P. & Palmquist, A. The Orientation of Nanoscale Apatite Platelets in Relation to Osteoblastic–Osteocyte Lacunae on Trabecular Bone Surface. *Calcif. Tissue Int.* **98**, 193–205 (2016).

13. Shah, F. A., Ruscsák, K. & Palmquist, A. Transformation of bone mineral morphology: From discrete marquise-shaped motifs to a continuous interwoven mesh. *Bone Reports* **13**, 100283 (2020).

14. Ottani, V., Martini, D., Franchi, M., Ruggeri, A. & Raspanti, M. Hierarchical structures in fibrillar collagens. *Micron* **33**, 587–596 (2002).

15. Shoulders, M. D. & Raines, R. T. Collagen Structure and Stability. *Annu. Rev. Biochem.* **78**, 929–958 (2009).

16. Canelón, S. P. & Wallace, J. M. β-Aminopropionitrile-induced reduction in enzymatic crosslinking causes in vitro changes in collagen morphology and molecular composition. *PLoS One* **11**, (2016).

17. Ramshaw, J. A. M., Shah, N. K. & Brodsky, B. Gly-X-Y Tripeptide Frequencies in Collagen: A Context for Host–Guest Triple-Helical Peptides. *J. Struct. Biol.* **122**, 86–91 (1998).

18. Reznikov, N., Shahar, R. & Weiner, S. Three-dimensional structure of human lamellar bone : The presence of two different materials and new insights into the hierarchical organization.

Bone **59**, 93–104 (2014).

19. Deshpande, A. S. & Beniash, E. Bioinspired synthesis of mineralized collagen fibrils. *Cryst. Growth Des.* **8**, 3084–3090 (2008).

20. Landis, W. J. & Silver, F. H. The structure and function of normally mineralizing avian tendons. *Comp. Biochem. Physiol. - A Mol. Integr. Physiol.* **133**, 1135–1157 (2002).

21. Su, X., Sun, K., Cui, F. Z. & Landis, W. J. Organization of apatite crystals in human woven bone. *Bone* **32**, 150–162 (2003).

22. Schwarcz, H. P., McNally, E. A. & Botton, G. A. Dark-field transmission electron microscopy of cortical bone reveals details of extrafibrillar crystals. *J. Struct. Biol.* **188**, 240–248 (2014).

23. Reznikov, N., Bilton, M., Lari, L., Stevens, M. M. & Kröger, R. Fractal-like hierarchical organization of bone begins at the nanoscale. *Science (80-.).* **360**, (2018).

24. Beniash, E., Metzler, R. A., Lam, R. S. K. & Gilbert, P. U. P. A. Transient amorphous calcium phosphate in forming enamel. *J. Struct. Biol.* **166**, 133–143 (2009).

25. Mahamid, J. *et al.* Mapping amorphous calcium phosphate transformation into crystalline mineral from the cell to the bone in zebrafish fin rays. *Proc. Natl. Acad. Sci. U. S. A.* **107**, 6316–6321 (2010).

26. Crenshaw, M. A. Mineral Induction by Immobilized Polyanions. *Mech. Phylogeny Miner. Biol. Syst.* **21**, 101–105 (1991).

27. Nudelman, F. *et al.* The role of collagen in bone apatite formation in the presence of hydroxyapatite nucleation inhibitors. *Nat. Mater.* **9**, 1004–1009 (2010).

28. Gorski, J. P. Biomineralization of bone: a fresh view of the roles of non-collagenous proteins. *Front. Biosci.* **16**, 2598 (2011).

29. George, A. & Veis, A. Phosphorylated proteins and control over apatite nucleation, crystal growth, and inhibition. *Chem. Rev.* **108**, 4670–4693 (2008).

30. Nudelman, F., Lausch, A. J., Sommerdijk, N. A. J. M. & Sone, E. D. In vitro models of collagen biomineralization. *J. Struct. Biol.* **183**, 258–269 (2013).

31. Price, P. A., Toroian, D. & Lim, J. E. Mineralization by inhibitor exclusion. The calcification of collagen with fetuin. *J. Biol. Chem.* **284**, 17092–17101 (2009).

32. Thula, T. T. *et al.* Mimicking the nanostructure of bone: Comparison of polymeric process-directing agents. *Polymers (Basel).* **3**, 10–35 (2011).

33. Nudelman, F., Bomans, P. H. H., George, A., De With, G. & Sommerdijk, N. A. J. M. The role of the amorphous phase on the biomimetic mineralization of collagen. *Faraday Discuss.* **159**, 357–370 (2012).

34. Thula, T. T. *et al.* In vitro mineralization of dense collagen substrates: A biomimetic approach toward the development of bone-graft materials. *Acta Biomater.* **7**, 3158–3169 (2011).

35. Jee, S. S., Kasinath, R. K., Dimasi, E., Kim, Y. Y. & Gower, L. Oriented hydroxyapatite in turkey tendon mineralized via the polymer-induced liquid-precursor (PILP) process. *CrystEngComm* **13**, 2077–2083 (2011).

36. Lausch, A. J., Quan, B. D., Miklas, J. W. & Sone, E. D. Extracellular Matrix Control of Collagen Mineralization In Vitro. *Adv. Funct. Mater.* **23**, 4906–4912 (2013).

37. Rodriguez, D. E. *et al.* Multifunctional role of osteopontin in directing intrafibrillar mineralization of collagen and activation of osteoclasts. *Acta Biomater.* **10**, 494–507 (2014).

38. Gower, L. B. *et al.* Biomimetic Approach Toward the Development of Bone-Graft. *Acta biomateralia* **7**, 3158–3169 (2012).

39. Goldstein, J. I. *et al. Microscopy and X-Ray Microanalysis*.

40. Ul-Hamid, A. *A Beginners' Guide to Scanning Electron Microscopy*. *A Beginners' Guide to Scanning Electron Microscopy* (Springer International Publishing, 2018). doi:10.1007/978-3-319-98482-7

41. Inkson, B. J. *Scanning Electron Microscopy (SEM) and Transmission Electron Microscopy (TEM) for Materials Characterization*. *Materials Characterization Using Nondestructive Evaluation (NDE) Methods* (Elsevier Ltd, 2016). doi:10.1016/B978-0-08-100040-3.00002-X

42. Egerton, R. F., Li, P. & Malac, M. Radiation damage in the TEM and SEM. *Micron* **35**, 399–409 (2004).

43. Williams, D. B. & Carter, C. B. Lenses, Apertures, and Resolution. in *Transmission Electron Microscopy* 85–104 (Springer US, 1996). doi:10.1007/978-1-4757-2519-3_6

44. ไทรทับทิม, ส. *No Title*การนำสาหร่ายที่ผลิตน้ำมันไบโอดีเซลมาบำบัดน้ำเสียของ โรงงานอุตสาหกรรมรีไซเคิล. (2554).

45. Liu, D. Features of the ISO-25498: Method of selected area electron diffraction analysis in transmission electron microscopy. *Microsc. Microanal.* **19**, 207–209 (2013).

46. Zhou, X. & Thompson, G. E. *Electron and Photon Based Spatially Resolved Techniques*. *Reference Module in Materials Science and Materials Engineering* (Elsevier Ltd., 2017). doi:10.1016/b978-0-12-803581-8.10140-7

47. Quorum. Quorum technologies user manual.

48. Berthomieu, C. & Hienerwadel, R. Fourier transform infrared (FTIR) spectroscopy. *Photosynth. Res.* **101**, 157–170 (2009).

49. Edition, S. CHAPTER I THEORETICAL BACKGROUND. *Acta Psychiatr. Scand.* **42**, 3–13 (1967).

50. Smith, B. C. *Fundamentals of fourier transform infrared spectroscopy, second edition*. *Fundamentals of Fourier Transform Infrared Spectroscopy, Second Edition* (2011).

51. Figueiredo, M. M., Gamelas, J. A. F. & Martins, A. G. Characterization of Bone and Bone-Based Graft Materials Using FTIR Spectroscopy. *Infrared Spectrosc. - Life Biomed. Sci.* (2012). doi:10.5772/36379

52. Mohamed, M. A., Jaafar, J., Ismail, A. F., Othman, M. H. D. & Rahman, M. A. *Fourier Transform Infrared (FTIR) Spectroscopy*. *Membrane Characterization* (Elsevier B.V., 2017). doi:10.1016/B978-0-444-63776-5.00001-2

53. Brangule, A. & Gross, K. A. Importance of FTIR spectra deconvolution for the analysis of amorphous calcium phosphates. *IOP Conf. Ser. Mater. Sci. Eng.* **77**, (2015).

54. France, C. A. M., Sugiyama, N. & Aguayo, E. Establishing a preservation index for bone, dentin, and enamel bioapatite mineral using ATR-FTIR. *J. Archaeol. Sci. Reports* **33**, 102551 (2020).

55. Sroka-Bartnicka, A., Borkowski, L., Ginalska, G., Ślósarczyk, A. & Kazarian, S. G. Structural transformation of synthetic hydroxyapatite under simulated in vivo conditions studied with ATR-FTIR spectroscopic imaging. *Spectrochim. Acta - Part A Mol. Biomol. Spectrosc.* **171**, 155–

161 (2017).

56. Rey, C., Shimizu, M., Collins, B. & Glimcher, M. J. Resolution-enhanced fourier transform infrared spectroscopy study of the environment of phosphate ion in the early deposits of a solid phase of calcium phosphate in bone and enamel and their evolution with age: 2. Investigations in thev 3 PO4 domain. *Calcif. Tissue Int.* **49**, 383–388 (1991).

57. Murugan, R., Ramakrishna, S. & Panduranga Rao, K. Nanoporous hydroxy-carbonate apatite scaffold made of natural bone. *Mater. Lett.* **60**, 2844–2847 (2006).

58. Habraken, W. J. E. M. *et al.* Ion-association complexes unite classical and non-classical theories for the biomimetic nucleation of calcium phosphate. *Nat. Commun.* **4**, (2013).

59. Olesik, J. W. Elemental analysis using ICP-OES and ICP/MS. *Anal. Chem.* **63**, 12A-21A (1991).

60. ICP-OES, 2019. https://www.ru.nl/science/gi/facilitiesactivities/elemental-analysis/icp-oes/.

61. Wang, T. Inductively coupled plasma optical emission spectrometry. *Anal. Instrum. Handbook, Third Ed.* 57–74 (2004). doi:10.1201/9781315118024-3

62. Chen, P. Y., Toroian, D., Price, P. A. & McKittrick, J. Minerals form a continuum phase in mature cancellous bone. *Calcif. Tissue Int.* **88**, 351–361 (2011).

63. Midura, R. J. *et al.* Calcospherulites11Calcospherulites (calco: calcium salt + spherulite: spherical crystalline body); calcium-containing, spherical bodies have also been referred to as calcified microspheres, mineral clusters, crystal ghost aggregates, calcification nodules. *Bone* **41**, 1005–1016 (2007).

64. Relucenti, M. *et al.* SEM BSE 3D Image Analysis of Human Incus Bone Affected by Cholesteatoma Ascribes to Osteoclasts the Bone Erosion and VpSEM dEDX Analysis Reveals New Bone Formation. *Scanning* **2020**, (2020).

65. Marotti, G. Osteocyte orientation in human lamellar bone and its relevance to the morphometry of periosteocytic lacunae. *Metab. Bone Dis. Relat. Res.* **1**, 325–333 (1979).

66. Callis, G. & Sterchi, D. Decalcification of Bone: Literature Review and Practical Study of Various Decalcifying Agents. Methods, and Their Effects on Bone Histology. *J. Histotechnol.* **21**, 49–58 (1998).

67. Boskey, A. & Pleshko Camacho, N. FT-IR imaging of native and tissue-engineered bone and cartilage. *Biomaterials* **28**, 2465–2478 (2007).

68. Bridelli, M. G., Stani, C. & Bedotti, R. Fourier transform infrared conformational investigation of type I collagen aged by in vitro induced dehydration and non-enzymatic glycation treatments. *J. Biol. Res.* **90**, 45–50 (2017).

69. Schwarcz, H. P., Abueidda, D. & Jasiuk, I. The ultrastructure of bone and its relevance to mechanical properties. *Front. Phys.* **5**, (2017).

70. Doublier, A., Farlay, D., Jaurand, X., Vera, R. & Boivin, G. Effects of strontium on the quality of bone apatite crystals: A paired biopsy study in postmenopausal osteoporotic women. *Osteoporos. Int.* **24**, 1079–1087 (2013).

71. Farlay, D., Panczer, G., Rey, C., Delmas, P. D. & Boivin, G. Mineral maturity and crystallinity index are distinct characteristics of bone mineral. *J. Bone Miner. Metab.* **28**, 433–445 (2010).

72. Akiva, A. *et al.* Intercellular pathways from the vasculature to the forming bone in the zebrafish larval caudal fin: Possible role in bone formation. *J. Struct. Biol.* **206**, 139–148

(2019).